https://doi.org/10.5194/egusphere-2025-6386
Preprint. Discussion started: 30 December 2025

Towards a parametric Kalman filter for operational wildfire plume assimilation: Formulation of the forecast step

Annika Vogel[1,2], Richard Ménard[1], James Abu[1], and Jack Chen[3]

[1]Air Quality Research Division, Environment and Climate Change Canada (ECCC), Dorval, Quebec, Canada
[2]Institute of Geophysics and Meteorology, University of Cologne, Cologne, Germany
[3]Air Quality Research Division, Environment and Climate Change Canada (ECCC), Ottawa, Ontario, Canada

Correspondence: Annika Vogel (annika.vogel@uni-koeln.de)

Abstract. This study introduces a simple parametric Kalman Filter (PKF) specifically tailored to the requirements of operational air quality data assimilation under highly uncertain emissions like wildfire smoke events. Operational smoke plume assimilation systems require fast, yet accurate error estimations to represent the large, case-dependent and spatio-temporally varying uncertainties. The PKF offers a computationally efficient alternative to existing ensemble approaches, where the dynamics of error parameters (such as error standard deviations) are explicitly evolved numerically at a fraction of the cost of ensemble-based methods. This study focuses on the forecast step of the PKF by evolving error standard deviations in the Canadian operational air quality model GEM-MACH. It includes the following three steps: 1) theoretical derivation of forecast dynamics tailored to near-surface air quality applications with uncertain emissions, 2) implementation into the GEM-MACH modeling system, 3) application to surface PM2.5 in eastern Canada during a wildfire episode in July 2023.

The theoretical investigation conducted in this study suggests that error standard deviation is a more suitable parameter than error variance for operational models. This is due to improved process-understanding, numerical accuracy, and a simpler form of the forecast equation that can be implemented with minor modifications of the forecasting model. Implementing diffusion and emission processes of errors in a state-of-the-science atmospheric model for the first-time demonstrates their sensitivity to other error parameters, state error correlation and emission error, respectively. Although the setup of the error forecast remains highly simplified, the case study results show significant impacts on hourly PM2.5 analysis increments compared to the operational setup. These differences can be related to the ability of the simple PKF to attribute large analysis increments to highly uncertain areas like wildfire plumes far away from observation locations. Thus, spreading sparse observation information much more efficiently in a highly case-dependent and anisotropic way only though improved variance fields.

1 Introduction

Air quality forecasting is a complex prognostic problem that includes several dynamical, physical and chemical processes in the atmosphere. Furthermore, the atmospheric composition is effected by other parts of the earth system e.g. via anthropogenic- and

https://doi.org/10.5194/egusphere-2025-6386
Preprint. Discussion started: 30 December 2025

natural emissions and deposition. In contrast to regular biogenic emissions from plants, wildfire emissions can be considered as rare and unexpected natural emission events with exceptionally high impacts on air quality, weather and humans (Byrne et al., 2024; Wang et al., 2024; Chen et al., 2025; Flood et al., 2025; Henderson, 2025; Zhang et al., 2025). Over the last years, record-breaking fire seasons in terms of numbers, area burned and socio-economic-environmental impacts have been raising the public attention as well as the demand for continuing research and improved forecasts. In Canada, the 2023 fire season was an unprecedented natural disaster with more than 15 million hectares (Mha) of forests consumed by wildfires (Jain et al., 2024). Smoke from wildfires resulted in extremely poor air quality across Canada and into the USA. Smoke plumes were also transported long-distances across the Atlantic impacting cities in Europe.

Active research in modeling and predicting the onset and development of fires based on environmental conditions (e.g. (e.g., Kaiser et al., 2012; Rochoux et al., 2015; Srivas et al., 2017; Zhou et al., 2021; Wu et al., 2024; Anderson et al., 2024) and latest satellite observations has resulted in considerable progress. However, especially the occurrence of new fires can only be predicted in a probabilistic sense and their estimated location, size, composition and evolution remain highly uncertain. Because air quality forecasts are highly dependent on emissions, especially large intermittent sources such as wildfires, emission uncertainties have large impact on the accuracy of the dispersion forecasts. In addition, these unexpected events often cover a large range of spatio-temporal scales with high variability and gradients, which makes dispersion forecasts for these events exceptionally challenging. Wildfire emission uncertainty extends to the vertical distribution of emissions in the atmospheric column as plume-injection heights. The model predictive skill for hundreds of km downwind of fire locations are highly sensitive to these parameters (Griffin et al., 2020; Ke et al., 2021). Moreover, fire spread and emission models rely on the latest satellite data which are only available in near real-time (e.g., Rochoux et al., 2013; Chen et al., 2019). Thus, the operational need for fast, yet reliable and accurate air quality forecasts become especially critical for wildfire smoke dispersion and other unexpected events.

These properties of wildfire smoke forecasts also induce specific challenges for air quality data assimilation and uncertainty quantification. The optimization of model states or parameters by data assimilation provides a sophisticated way to improve air quality forecasts in an operational setup. However, the optimal analysis determined by data assimilation highly relies on an accurate representation of forecast uncertainties. Forecast uncertainties generally vary in space and time, but background error estimates used in operational air quality assimilation systems are usually highly simplified due to its high dimensionality, error complexity and the leak of knowledge. These simplified error formulations often assume uniform error properties or statistical relations (e.g., Ménard and Deshaies-Jacques, 2018a; Sun et al., 2020; Colette et al., 2025), including a recent wildfire smoke application by Wang et al. (2025), which are not able to represent their complex error dynamics inducing highly variable, non-uniform and anisotropic errors and their correlations. This highly case-specific nature of unexpected emission events requires a non-statistical formulation of errors that accounts for their specific spatio-temporal error dynamics.

In contrast, the use of ensemble forecasts has proven its ability to account for highly complex non-linear error dynamics in various atmospheric applications, mostly in numerical weather prediction (NWP) systems. Despite its great success in meteorology, ensemble methods have a few disadvantages when applied to air quality forecasting systems: Firstly, the creation

https://doi.org/10.5194/egusphere-2025-6386
Preprint. Discussion started: 30 December 2025

of an appropriate ensemble that represents the true forecast uncertainties is not straight-forward. In contrast to NWP, model parameters like emission or deposition rates are an substantial source of uncertainties in air quality forecasts. Especially for natural emissions which are themselves calculated from emission models, uncertainties in air quality forecast can arise from many different sources with unknown error features (e.g., Vogel and Elbern, 2021a). All of these possible error sources their respective input uncertainties need to be appropriated by the ensemble (e.g., Vogel and Elbern, 2021b). Moreover, Sabathier et al. (2023) demonstrated challenges in creating consistent ensemble perturbations at boundary conditions.

Secondly, together with the high dimension of the model, this complexity of uncertainties induces the need for a large ensemble sizes. In operational NWP and air quality systems, large ensembles of 50 to 100 simulations and respective expensive computational demands motivated large efforts into advanced ensemble methods (e.g., Buehner et al., 2015; Park et al., 2022; Pendergrass et al., 2023). Thirdly, even these large ensemble sizes are orders of magnitude smaller than the degrees-of-freedom in the atmospheric system (usually 10^6 to 10^8). Thus, the sampling covariance calculated from the ensemble is highly underdetermined (e.g., Leutbecher, 2019) and resulting sampling errors induce new scientific challenges like localization and inflation to avoid ensemble collapse. While the two latter disadvantages and related methods described above have mostly been investigated for NWP systems, air quality models usually have larger state dimensions, and thus even increased ensemble sizes and potential sampling problems (Kong et al., 2021; Park et al., 2022).

Recently, fast-developing machine leaning methods have also been applied to estimate forecast uncertainties (e.g., Sacco et al., 2022; Brecht and Bihlo, 2023; Li et al., 2024; Sitwell, 2025). While these studies show promising results in terms of computational efficiency in the application, the training process can be very expensive as it requires large amounts of forecast and related uncertainty data. Additionally, the performance highly relies on the accuracy of uncertainties in the training data which again needs to be estimated.

Given these disadvantages of existing data assimilation methods, this study explores an alternative approach to estimate complex case-dependent forecast uncertainties for air quality data assimilation using a parametric formulation. This method does not aim at replacing existing methods in general, but rather provides an alternative with focuses on the operational need for fast and accurate air quality data assimilation. The underlying idea is to explicitly formulate equations for selected error parameters, which was initiated by Epstein (1969); Cohn (1993). These parameters describe the leading moments of the uncertainty distribution around the model state, e.g. error variance and correlation length scales for a Gaussian distribution. In a Kalman filter-based assimilation system, this Parametric Kalman Filter (PKF) consists of the equations for the change of the error parameters during the analysis and forecast step. The explicit derivation of prognostic equations of error parameters in a PKF system provides unique insights into the specific error dynamics in the system.

Previous studies for idealized atmospheric applications have shown that the consideration of a few error parameters is able to represent the dynamics of complex error features with considerably reduced computational loads compared to ensemble approaches. The first applications to an idealized atmospheric system are provided by Pannekoucke et al. (2016, 2018) who demonstrate the accuracy of a PKF compared to a full Kalman Filter (KF) and ensemble Kalman Filter (EnKF) for one-dimensional univariate advection-diffusion systems. Recently, Perrot et al. (2023) generalized the idealized experiments to a

https://doi.org/10.5194/egusphere-2025-6386
Preprint. Discussion started: 30 December 2025

multivariate formulation of up to 6 interacting chemical tracers including cross-tracer error covariance and correlation. Their idealized experiments also demonstrate high accuracy of the multivariate PKF compared to an enKF with 1600 members for highly nonlinear error dynamics. In addition to these studies, the very first real-case applications with a variance-only evolving scheme were used in stratospheric chemical data assimilation Ménard and Chang (2000); Khattatov et al. (2000); Eskes et al. (2003), and in the free troposphere with the assimilation of methane in a hemispheric chemical transport model Voshtani et al. (2022).

This study introduces a simple PKF which is suitable for operational assimilation in a state-of-the-science air quality forecast model with special focus on high-emission applications like wildfire smoke events. The developments focus on the forecast step which requires the evolution of error parameters within the air quality model. The operational need for fast, yet accurate error estimation motivates the development of a simple formulation of the PKF which can be easily implemented in complex high-dimensional systems. Therefore, only the first moment of error distributions, the error variance or standard deviation, is considered and its propagation restricted to the most important processes. A discussion of the selection of theses process and the theoretical formulation of the related prognostic error equations are given in Sec. 2. The presented PKF forecast step is then implemented into the coupled meteorology-air quality model GEM-MACH (Global Environmental Multi-scale – Modeling Air quality and CHemistry) and applied to PM2.5 in a case study during a wildfire smoke event in eastern Canada in July 2023. Sec. 3 provides an introduction to the GEM-MACH modeling system including the implementation and input of the error parameter forecast. The results of the Canadian wildfire case study with focus on the error forecasts and impacts on analysis increments from surface stations are presented in Sec. 4 and conclusions are given in Sec. 5.

2 Theoretical Formulation

The prognostic equation for the propagation of error parameters in a dynamical model depends on the prognostic equation of the related state. In large-scale numerical air-quality models, the temporal evolution of a 3D state concentration field $\xi_i(\mathbf{x},t)$ of species i at location $\mathbf{x} := [x,y,z]^T$ and time t can be written as advection-diffusion-reaction equation of the following general form:

$$\partial_t \xi_i(\mathbf{x},t) = -\mathbf{u}(\mathbf{x},t)\cdot\nabla\xi_i(\mathbf{x},t) + \nabla\Big(\boldsymbol{\kappa}(\mathbf{x},t)\cdot\nabla\xi_i(\mathbf{x},t)\Big) + \mathcal{P}_i\Big(\xi(\mathbf{x},t)\Big) + E_i(\mathbf{x},t) - D_i\Big(\xi_i(\mathbf{x},t)\Big) \tag{1}$$

with $\mathbf{u}(\mathbf{x},t)$ the 3D wind vector field, $\boldsymbol{\kappa}(\mathbf{x},t)$ the 3D diffusion tensor, $\mathcal{P}_i\Big(\xi(\mathbf{x},t)\Big)$ the total chemical net production or loss of species i from all other species, $E_i(\mathbf{x},t)$ the total emissions of species i, and $D_i\Big(\xi_i(\mathbf{x},t)\Big)$ the total deposition/sedimentation of species i. Note that each of this general processes may include multiple sub-processes in a complex air-quality model, thus the formulation in Eq. (1) is a highly simplified representation of the complete model. In the following, the species subscript i is dropped for simplicity.

Based on this general prognostic state equation, the prognostic equation for error parameters can be derived using their respective definitions. This study focuses on the first moment of an error distribution, which is the error variance or standard deviation. Assuming unbiased errors, the random additive error $\epsilon_\xi(\mathbf{x},t)$ of the state concentration field $\xi(\mathbf{x},t)$ is defined as its

https://doi.org/10.5194/egusphere-2025-6386
Preprint. Discussion started: 30 December 2025

difference to the unknown true state $\xi^t(\mathbf{x},t)$:

$$\epsilon_\xi(\mathbf{x},t) := \xi(\mathbf{x},t) - \xi^t(\mathbf{x},t) \tag{2}$$

With this, the concentration error variance $V_\xi(\mathbf{x},t)$ is defined as:

$$V_\xi(\mathbf{x},t) := \overline{\left(\epsilon_\xi(\mathbf{x},t)\right)^2} \tag{3}$$

And the concentration error standard deviation $\sigma_\xi(\mathbf{x},t)$ is defined as square root of the error variance:

$$\sigma_\xi(\mathbf{x},t) := \sqrt{V_\xi(\mathbf{x},t)} = \sqrt{\overline{\left(\epsilon_\xi(\mathbf{x},t)\right)^2}} \tag{4}$$

Thus, the prognostic equation for the error parameters can be derived from the equation of the error itself. The latter needs to be derived from the prognostic equation of the state and is therefore depending on the specific forecast model in Eq. (1). Given the enormous complexity of air quality models, the prognostic equations for error parameters will be restricted to a few processes which are considered to be most important for this application.

For the application to wildfire related air quality in this study, advection, vertical diffusion and point emissions are selected based on a preceding study Vogel et al. (2026) and theoretical considerations: Firstly, advection is a critical process for transport the plumes from their source region to impacted downwind areas. Secondly, vertical diffusion is particularly important for surface near the mixing within the boundary layer. Note that no physical horizontal diffusion is considered as most grid models including GEM-MACH, assuming numerical diffusion to be dominating in the horizontal. Thirdly, emissions are generally considered to be the most important and uncertain process in near-surface air quality modeling. Due to the focus on wildfires, point emissions are considered here, which include wildfire and anthropogenic point sources in GEM-MACH in contrast to gridded flux emissions from area sources.

The preceding study confirmed the minor impact of area emissions on the forecast of PM2.5 concentration in the vicinity of wildfire plumes for the specific smoke episode investigated in this study (compare Sec. 4.1). In addition, some theoretical arguments motivated the neglection of other processes: For deposition of sedimentation, the assumption of highly correlated errors that is used in the derivation of emission errors (see Sec.2.3 and Apx. A6) is more significantly violated. This makes the derivation of the change of error parameters due to deposition more challenging and will be investigated in a separate study. Generally, the deposition process is expected to reduce the absolute error due to reduced concentrations, while an uncertainty in the deposition parameter would act as a source of uncertainty. For this study, it is assumed that these two opposing aspects approximately cancel out resulting in a minor overall impact on error parameters.

Including chemical conversions in the forecast of error parameters require the consideration of the error parameters of all other species involved. This is conceptually feasible as demonstrated by Perrot et al. (2023), it requires however much more computational effort because of the increased number of error parameters. Moreover, the coupling of multiple error parameters makes the interpretation of the results much more complex which is contrary to the scope of this study of a simple PKF for operational use. For this specific application of PM2.5 in wildfire smoke episodes, the concentration field of total PM2.5 is assumed to be approximately chemically inactive for the time period of a few days.

https://doi.org/10.5194/egusphere-2025-6386
Preprint. Discussion started: 30 December 2025

In the following, Sec. 2.1 to 2.3 derive the prognostic equations for the three considered processes, respectively, for both parameters, error variance and standard deviation. A special focus is given to the two new processes for real-case applications; diffusion and emissions, for which the formulations of variance and standard deviation are compared and evaluated with respect to implementation into complex operational models. The derivations of the equations in this section are provided in Apx. A, the related equation numbers are given in brackets above the equal-signs.

2.1 Advection

The 3D advection of a concentration field $\xi(\mathbf{x},t)$ is given by:

$$\partial_t \xi(\mathbf{x},t)\Big|_{\text{adv}} \overset{(1)}{=} -\mathbf{u}(\mathbf{x},t)\cdot\nabla\xi(\mathbf{x},t) \tag{5}$$

Assuming a true 3D wind vector field $\mathbf{u}(\mathbf{x},t)$, the propagation of the error field $\epsilon_\xi(\mathbf{x},t)$ is reduced to the original prognostic equation:

$$\partial_t \epsilon_\xi(\mathbf{x},t)\Big|_{\text{adv}} \overset{(A8)}{=} -\mathbf{u}(\mathbf{x},t)\cdot\nabla\epsilon_\xi(\mathbf{x},t) \tag{6}$$

And with the definition of error variance, its propagation due to advection becomes:

$$\partial_t V_\xi(\mathbf{x},t)\Big|_{\text{adv}} \overset{(A11)}{=} -\mathbf{u}(\mathbf{x},t)\cdot\nabla V_\xi(\mathbf{x},t) \tag{7}$$

Similarly, the propagation of error standard deviation due to advection:

$$\partial_t \sigma_\xi(\mathbf{x},t)\Big|_{\text{adv}} \overset{(A14)}{=} -\mathbf{u}(\mathbf{x},t)\cdot\nabla\sigma_\xi(\mathbf{x},t) \tag{8}$$

For a derivation of the advection equations Eq. (6)-(8) see Apx. A3 or Pannekoucke et al. (2018), their Sec.3.2.2.

The propagation of both, error variance and standard deviation due to advection is described in the same form as the state advection. Thus, the models advection scheme can be used for either error parameter without any modifications required. Note also that although the advection equation is exact, the potential errors due to dynamical uncertainties in the wind field and numerical errors in the discrete advection scheme impact advection of error parameters in the way same as state concentrations.

2.2 Vertical diffusion

This study only considers 1D vertical diffusion like most grid models including GEM-MACH in which numerical diffusion is assumed to be dominating in the horizontal (for more details see Sec. 4).

The 1D diffusion of a concentration field $\xi(\mathbf{x},t)$ into vertical direction z is given by:

$$\partial_t \xi(\mathbf{x},t)\Big|_{\text{vdiff}} \overset{(1)}{=} \partial_z\Big(\kappa^z(\mathbf{x},t)\cdot\partial_z\xi(\mathbf{x},t)\Big) \tag{9}$$

Assuming true vertical diffusion coefficient field $\kappa^z(\mathbf{x},t)$, the propagation of the unbiased random error field $\epsilon_\xi(\mathbf{x},t)$ is reduced to the original prognostic equation (for derivation see e.g. Pannekoucke et al. (2018), their Eq.(15c)):

$$\partial_t \epsilon_\xi(\mathbf{x},t)\Big|_{\text{vdiff}} \overset{(A15)}{=} \partial_z\Big(\kappa^z(\mathbf{x},t)\cdot\partial_z\epsilon_\xi(\mathbf{x},t)\Big) \tag{10}$$

https://doi.org/10.5194/egusphere-2025-6386
Preprint. Discussion started: 30 December 2025

And with the definition of error variance, its propagation by vertical diffusion becomes:

$$\partial_t V_\xi(\mathbf{x},t)\Big|_{\text{vdiff}} \overset{(A24)}{=} \underbrace{\partial_z\Big(\kappa^z(\mathbf{x},t)\cdot\partial_z V_\xi(\mathbf{x},t)\Big)}_{\text{(I) standard phy. diff.}} \underbrace{-2\,\kappa^z(\mathbf{x},t)\cdot V_\xi(\mathbf{x},t)\cdot\Big(L_\xi^z(\mathbf{x},t)\Big)^{-2}}_{\text{(II) correlation term}} \underbrace{-2\,\kappa^z(\mathbf{x},t)\cdot V_\xi(\mathbf{x},t)\cdot\left(\frac{\partial_z V_\xi(\mathbf{x},t)}{2\,V_\xi(\mathbf{x},t)}\right)^2}_{\text{(III) gradient term}} \tag{11}$$

with $L_\xi^z(\mathbf{x},t)$ the error correlation length in vertical direction z.

Note that the change of error variances due to vertical diffusion includes two additional terms in addition to the "standard physical diffusion term" that describes state diffusion: a "correlation term" which describes the reduction of error variance due to the diffusion of a spatially finite-correlated state, and a "gradient term" which describes the change of error variance as function of its normalized spatial gradient. For an idealized example of the individual terms see Apx. B1. For a derivation of the diffusion equations Eq. (10)-(11) see Apx. A4 or Pannekoucke et al. (2018), their Sec.3.2.3.

Similarly, the propagation of error standard deviation by vertical diffusion becomes:

$$\partial_t \sigma_\xi(\mathbf{x},t)\Big|_{\text{vdiff}} \overset{(A27)}{=} \underbrace{\partial_z\Big(\kappa^z(\mathbf{x},t)\cdot\partial_z \sigma_\xi(\mathbf{x},t)\Big)}_{\text{(I) standard phy. diff.}} \underbrace{-\kappa^z(\mathbf{x},t)\cdot\sigma_\xi(\mathbf{x},t)\cdot\Big(L_\xi^z(\mathbf{x},t)\Big)^{-2}}_{\text{(II) correlation term}} \tag{12}$$

which is derived in Apx. A5.

In addition to the standard physical diffusion term, the correlation term additionally reduces error standard deviation due to diffusion of finite-correlated state concentrations and the amount of this reduction increases with decreasing vertical error correlation length $L_\xi^z(\mathbf{x},t)$. Thus the change of both, error variance and standard deviation, depend on two parameters: the vertical diffusion coefficient and the vertical error correlation length. Here, the latter is not considered as prognostic variable in the model and must therefore be chosen as model parameter. Apx. B2 demonstrates the high sensitivity of the error variance forecast to the formulation of error correlation length in an idealized 1D experiment.

Despite the mathematical equivalence of the two formulations in Eq. (11)-(12), the standard deviation form of the diffusion equation appears to have some practical advantages compared to the error variance form when it comes to applications in complex operational models:

- Standard deviation has the same unit as the original quantity which becomes beneficial in the implementation and interpretation of results.
- Standard deviation fields can be assumed to have a higher numerical stability because they have lower ranges of values and smaller gradients than variance fields (being the square of standard deviation).
- The diffusion equation for standard deviation in Eq. (12) avoids the calculation of the third term (compare Eq. (11)). This becomes a big advantage in complex models because it does not only reduces the computations by one term (two

https://doi.org/10.5194/egusphere-2025-6386
Preprint. Discussion started: 30 December 2025

instead of three terms), but it also avoids the numerical calculation of an additional spatial derivative in the gradient term which indices additional discretization errors.

– The simpler equation for standard deviations also allows generally a more intuitive interpretation of the processes in the equation (see Apx. B1) as well as an easier verification of the actual model code.

Therefore, error standard deviation was selected as prognostic variable in the model, and is the main quantity described in the remaining document. The differences between the two forms are illustrated in Apx. B1 for an idealized 1D experiment using pure diffusion.

2.3 Point emissions

Conceptually, emissions are an external source that add to local concentrations independently of the state. In air quality models like GEM-MACH, emissions are often implemented in two different ways: point sources, including wildfires, are pre-calculated for each gridbox and added to the respective concentrations as individual process. In contrast, area sources are included in as additional flux term in the generalized diffusion equation. This conceptually different treatment of emissions requires a separate consideration for error parameters. Here, only point emissions are considered at this stage, due to simplicity and focus on wildfires, the importance of which were verified by Vogel et al. (2026).

The change of state concentrations due to point emissions of each species is given by the respective emission field $E(\mathbf{x},t)$:

$$\partial_t \xi(\mathbf{x},t)\Big|_{\text{p.emis}} \overset{(1)}{=} E(\mathbf{x},t) \tag{13}$$

With this, the concentration error due to uncertainties in this prescribed emission field $E(\mathbf{x},t)$ is given by its deviation from the true emission field $E^t(\mathbf{x},t)$:

$$\partial_t \epsilon_\xi(\mathbf{x},t)\Big|_{\text{p.emis}} \overset{(A29)}{=} E(\mathbf{x},t) - E^t(\mathbf{x},t) \quad := \epsilon_E(\mathbf{x},t) \tag{14}$$

with $\epsilon_E(\mathbf{x},t)$ the random additive emission error under the assumption of unbiased emissions.

The derivation of the equations for error parameters in Apx. A6 requires an assumption about the correlation between local state and emission errors. The state concentration at emission locations is often highly dominated by the local emissions, especially for high emission events like wildfires, and so are their errors.

Thus, assuming highly correlated errors, the error variance of the state can be approximated by:

$$\partial_t V_\xi(\mathbf{x},t)\Big|_{\text{p.emis}} \overset{(A33)}{\approx} 2\,\sigma_\xi(\mathbf{x},t)\cdot\sigma_E(\mathbf{x},t) \tag{15}$$

Similarly, the error standard deviation of the state can be approximated by:

$$\partial_t \sigma_\xi(\mathbf{x},t)\Big|_{\text{p.emis}} \overset{(A36)}{\approx} \sigma_E(\mathbf{x},t) \tag{16}$$

The derivation of the emission equations Eq. (14)-(16) is given in Apx. A6.

https://doi.org/10.5194/egusphere-2025-6386
Preprint. Discussion started: 30 December 2025

Consequently, the concentration error standard deviation or variance can only be increased by emissions, but only if the emissions are considered to be uncertain. The emission error standard deviation can therefore be interpreted as source of uncertainty in the prognostic error field, similar to emissions as source of concentration.

It can be seen from Eq. (16) that the change in concentration error standard deviation due to emissions is equal to the emission error standard deviation. Thus providing again a simpler formulation than the one of error variance Eq. (15) which includes the state standard deviation on the right hand side. This facilitates the implementation in a complex numerical model and reduces the numerical complexity from quadratic to linear (see Apx A6: Eq. (A37)-(A38)). Moreover, because of its equivalence to the state equation in Eq. (13), the original code for state emissions which are added to state concentrations can also be used when adding emission error standard deviation to concentration error standard deviations. The fact that standard deviations have the same unit as concentrations becomes another advantage here (compare Sec. 2.2).

3 Implementation

This section describes the implementation of the PKF forecast equations for error standard deviations of Sec. 2 into the regional operational version of the coupled meteorology-air quality model GEM-MACH.

3.1 Current modeling system

The coupled meteorology-air quality model GEM-MACH (Global Environmental Multiscale - Modeling Air quality and CHemistry) is developed and operationally maintained at Environment and Climate Change Canada (ECCC). It includes one-way coupling of meteorology and chemical processes, where atmospheric chemical compositions is calculated on-line as part of numerical weather prediction model forecast, but do not influence, or feedback, the forecast weather processes. The operational regional GEM-MACH system RAQDPS-FW (Regional Air Quality Deterministic Prediction System with Near-Real-Time Wildfire Emissions, ECCC RAQDPS (technote: https://eccc-msc.github.io/open-data/msc-data/nwp_raqdps/readme_raqdps_en) covers north America with a 10km horizontal resolution and 84 vertical layers in hybrid coordinates from the surface to 0.1hPa. This system, also known as FireWork, includes the Canadian Forest Fire Emission Prediction System (CFFEPS), which provides near-real-time wildfire emissions with satellite-based fire hotspot information (Chen et al., 2019).

The current system does not include horizontal diffusion as dynamical processes. This is due to the fact that the horizontal grid size is much larger than the length-scale of the physical diffusion and thus numerical diffusion is the primary diffusion mechanism in the horizontal direction. Numerical diffusion results from error terms of the discrete diffusion scheme in the model as function of the spatial discretizations. Although this is fundamentally different from physical diffusion in the atmosphere, it impacts the forecast state in a similar way.

The setup of the new parametric error forecast presented in this study is compared to the operational setup for air quality analysis at ECCC. Currently, an hourly surface analysis is performed for selected species including PM2.5. The latest version of this objective analysis framework OAv2 (Objective Analysis version 2, Ménard et al., 2020) exploits statistical relations between local background concentrations and error variances at observation locations. The OAv2 calculates differences be-

https://doi.org/10.5194/egusphere-2025-6386
Preprint. Discussion started: 30 December 2025

tween station observations and related background values at each observation time and location during a 2 month running time period. Assuming Innovation (Co)variance Consistency (ICC), the innovation variances calculated from these differences w.r.t. time and location are approximately the sum of background- and observation error variance. Note that this assumes common error statistics over all observation locations and times though the considered domain. Given this, the estimated background error variances at the station locations are plotted against the background state and binned accordingly. These bins are then used to calculate a piecewise fit relation between background state concentrations and error variances with constant variances outside the state concentration range ("bounded piecewise fit", compare Sec. 3.3, Fig. 1). In the operational OAv2, this state-to-variance relation is applied to averaged background concentrations over 2 months running time period to get monthly estimates of background error variances that are used in the analysis.

In this study, the OAv2 framework is used as testbed for the case-study application of the PKF error estimates that were forecasted with GEM-MACH. The original OAv2 statistical error estimation serves as reference for comparison and a modification of the state-to-variance relation approach is used to provide input fields for the PKF-based estimates as described in Sec. 3.3.

3.2 Forecast implementation

Error standard deviation is added as additional prognostic field in the operational regional version of the GEM-MACH forecasting system. For the application to wildfire plumes, PM2.5 was selected as species of interest for which a error forecast is to be performed. PM2.5 is not a prognostic variable in GEM-MACH, but rather the sum of seven prognostic aerosol species and thus evolves with the same dynamical processes, advection and vertical diffusion, and the net chemical processes of the individual species. These chemical processes include anthropogenic- and wildfire point emissions, area emissions, chemical reactions and deposition.

As described in the introduction of Sec. 2, the related forecast of error standard deviation has a simplified formulation which only considers the most dominant changes due to advection, vertical diffusion and point emissions which need to be included in the forecast model. Firstly, the change of PM2.5 error standard deviation due to advection in Eq. (8) has the same form as the advection equation of the state. This means that this prognostic field can simply be handled by the original advection scheme like any concentration field in the model.

Secondly, the change of PM2.5 error standard deviation due to vertical diffusion in Eq. (12) differs from the vertical diffusion equation for concentration fields. For the first term which equals the diffusion processes of concentrations, the standard diffusion scheme of the model code can be used without any modifications. The second term describing the reduction of error standard deviation due to diffusion consists of a simple multiplication of scalars which need to be added at each location. This term is embedded into the vertical diffusion scheme of GEM-MACH which solves a generalized diffusion equation of the following form:

$$\partial_t \psi(\mathbf{x},t) = \left\{ \partial_z \left[\kappa(\mathbf{x},t) \Big(\partial_z \psi(\mathbf{x},t) + G_\psi(\mathbf{x},t) \Big) + J_\psi(\mathbf{x},t) \right] + R_\psi(\mathbf{x},t) \right\} \cdot F_\psi(\mathbf{x},t) \tag{17}$$

with ψ the prognostic field to be diffused and G_ψ, J_ψ, R_ψ, F_ψ related spatio-temporal parameters that allow for its generalized diffusion. While $G_\xi = J_\xi = R_\xi = 0$ and $F_\xi = 1$ reduce Eq. (17) to standard diffusion for each state concentration field ξ in

https://doi.org/10.5194/egusphere-2025-6386
Preprint. Discussion started: 30 December 2025

Eq. (9), an inhomogeneous term $R_\sigma \neq 0$ is applied to the error standard deviation field $\sigma_\xi(\mathbf{x},t)$ to fulfill Eq. (12):

$$R_\sigma(\mathbf{x},t) = -\kappa^z(\mathbf{x},t) \cdot \sigma_\xi(\mathbf{x},t) \cdot \left(L_\xi^z(\mathbf{x},t)\right)^{-2} \tag{18}$$

While the implementation of the additional term requires only minor code modifications, it includes the vertical error correlation length $L_\xi^z(\mathbf{x},t)$ as additional parameter which definition is not straight-forward. As described above, horizontal diffusion is not explicitly considered in the operational regional GEM-MACH and thus also not in the error standard deviation forecast (see also Sec. 5).

Thirdly, the change of PM2.5 error standard deviation due to uncertain point emissions in Eq. (16) is given by their emission error standard deviation. Thus, the emission error standard deviation is implemented as local source term for concentration error similarly to the state emissions as source term for state concentrations. Given the spatio-temporal emission error standard deviations, they will be treated as point emissions of the respective concentration error standard deviation in the original point emission scheme of the model. The critical part of this implementation is the appropriate formulation of emission error standard deviations which will be discussed below.

3.3 Input preparation

Like any other prognostic field in the model, the PM2.5 error standard deviation field needs initial- and boundary conditions to be propagated in the model. Here, the statistical estimation of background error variances in the current operational OAv2 is used to provide input estimates of error standard deviations. However, applying the statistical state-to-variance function from the OAv2 suite to the selected wildifre case study reveals the following problem: State concentrations of PM2.5 during wildfire episodes are orders of magnitude larger than the upper bound of the piecewise fit which is based on long-term averaged concentrations (e.g. for this case study, the upper PM2.5 concentration bound of 8.65 $\mu g\,m^{-3}$ is reached at 22 layers up to 3.000 m height, with a maximum surface concentration of 1972.5 $\mu g\,m^{-3}$). Thus, the resulting surface field of PM2.5 error variances is constant at the upper bound throughout large parts of the domain.

This is unfavorable for the following reasons: Firstly, the initial conditions for error standard deviation would be constant throughout most of the domain without any variations or gradients in the regions of smoke plumes which is contradictory to the goal of reproducing complex case-dependent forecast uncertainties. Secondly, it can be assumed that uncertainties are exceptionally large in wildfire smoke regions because their emissions estimates can be extremely variable and highly uncertain. Thirdly, Eq. (16) shows that concentration error standard deviation should increase in areas of highly uncertain emissions. Thus, state uncertainties can be assumed to be significantly locally increased within wildfires smoke plumes because of their exceptionally uncertain emission estimates which is not fulfilled by the operational setup. Moreover, any bounded state-to-variance relation for concentrations violates the emission-to-concentration consistency requirement: In order to ensure consistency in the error standard deviation forecast, emission-related sources of uncertainty should have the same impact on the prognostic error field, whether they are emitted within (as emissions) or before (as initial condition) the simulation period. For a bounded relation for initial- and boundary conditions, uncertain emissions further increase state error standard deviations beyond the

https://doi.org/10.5194/egusphere-2025-6386
Preprint. Discussion started: 30 December 2025

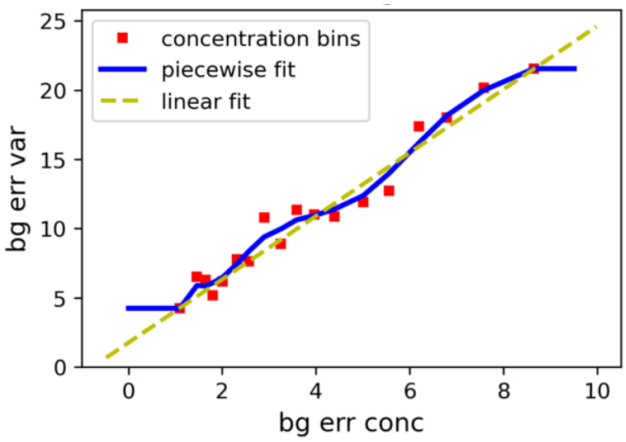

Figure 1. Example of fit functions for background error variances (in $(\mu g\,m^{-3})^2$) as function of background state concentrations (in $\mu g\,m^{-3}$) of PM2.5. Red squares: bins (mean values over each concentration bin, from cross-validation at obs stations), Blue solid line: bounded averaged piecewise linear fit used in OAv2. Yellow dashed line: Simple linear fit used in PKF.

upper bound within the simulation period, but not before the period or outside of the domain. This inconsistency still remains when emission variances are also bounded because they still add-up over time in the forecast.

To improve the input fields for PM2.5 error standard deviation w.r.t. these aspects, a simple linear fit of the state-to-variance function has been implemented which is given by the mean slope α_ξ and the offset β_ξ of the concentration bins. This linear state-to-variance relation is applied to the initial- and boundary fields of PM2.5 concentrations of this case study $\xi(\mathbf{x},t)$ to get case-specific estimates of the related input fields of PM2.5 concentration error standard deviation $\sigma_\xi(\mathbf{x},t)$:

$$\sigma_\xi(\mathbf{x},t) = \sqrt{V_\xi(\mathbf{x},t)} \approx \sqrt{\alpha_\xi \cdot \xi(\mathbf{x},t) + \beta_\xi} \tag{19}$$

Here, PM2.5 concentrations are calculated as sum over the seven individual prognostic fields of fine aerosol: elemental carbon, primary carbon, organic carbon, nitrate, sulfate, ammonium and crustal material. Figure 1 shows the bounded piecewise and linear fit for state-to-variance relations of PM2.5 concentrations used in this case study. Eq. (19) only applies to concentration fields like initial- and lateral boundary conditions, because they have the same quantity as the prognostic field.

For point emissions, the linear relation between emissions and concentrations (compare Sec. 2.3) allows the use of the same slope $\alpha_E = \alpha_\xi$, which also retains emission-to-concentration consistency discussed above. However, this does not hold for the offset, for which a conversion depends e.g. on the specific distribution of emissions into different vertical levels. Assuming that the offset is not as dominant as the linear slope, the emission error standard deviations are estimated from the linear slope with zero offset:

$$\sigma_E(\mathbf{x},t) = \sqrt{V_E(\mathbf{x},t)} \approx \sqrt{\alpha_E \cdot E(\mathbf{x},t)} \tag{20}$$

where $E(\mathbf{x},t)$ are the spatio-temporal fields of PM2.5 state emissions as sum of the seven aerosol components.

https://doi.org/10.5194/egusphere-2025-6386
Preprint. Discussion started: 30 December 2025

In contrast to the OAv2 where this fit is again applied to a 2 month running mean concentration field, it is here applied to the instant concentration field at each location to already include some state-dependency of errors in the input fields.

4 Case Study Application

The PM2.5 error standard deviation forecast in GEM-MACH is applied to a wildifre smoke episode in a preliminary case study. The purpose of this case study is not to provide a detailed case analysis, but rather to provide an initial proof of concept and exemplary demonstration of potential impacts and benefits of parametric error estimates in an air quality assimilation system compared to the current setup. This section includes the description of the case study and the simulation setup in Sec. 4.1, and the results of error standard deviations and analysis increments in Sec. 4.2 and Sec. 4.3, respectively. The results of the parametric experiments presented in this section are calculated with a vertical error correlation length of 6 model layers (approx. 385 m height at the surface over flat terrain). This value was selected from comparison of different vertical error correlation lengths discussed in Apx. C.

4.1 Case Study Description and Model Setup

Starting on June 5th 2023, a set of strong wildfires occurred in central Quebec, in eastern Canada. Despite wildfire sources were located far away from large cities, their smoke plumes were transported southwards reaching the highly populated regions in southern Quebec, Toronto and into northern USA, fumigating New York City within one to two days.

This study focuses on the core phase of the wildfire episode on June 6th 2023 where the main large-scale transport happened, the initial smoke plume reached Montreal and Ottawa, while wildfire continued in sources much further north producing emissions transported impacting southern regions. Figure 2 shows the temporal evolution of PM2.5 surface concentrations simulated by the regional GEM-MACH which serve as background concentrations in the hourly assimilation. The simulation was initialized on June 4th 00 UTC with a 24 hour forecast spinup. From June 5th 00 UTC three subsequent simulations of 12 hours each were performed to include updates to the most recent meteorological fields by operational IAU (Incremental Analysis Update)-assimilation and wildfire emissions from CFFEPS. For all results, the simulation is performed for the complete operational regional domain covering north America (denoted as "simulation domain" thereafter), but only part of it shown here focusing on eastern Canada from central Quebec to US border (denoted as "study domain" thereafter).

The PM2.5 concentration forecast shows several strong plumes related to wildfire hotspots in central Quebec. The largest surface concentrations are induced by the two large wildfires that are the most north. Besides that, two groups of smaller, but almost similarly strong wildfires can be found in along the Saguenay Fjord in the eastern center, and west of Gouin Reservoir in the western center of study domain. Further south, an old smoke plume that has been emitted the day before induces high PM2.5 concentrations around the urban areas of Ottawa, Montreal and into the US.

The forecasts of PM2.5 concentration and error standard deviation are used in the operational OAv2 suite estimating hourly surface analyses w.r.t. all available surface stations in the simulation domain. The setup of the OAv2 suite is equal to the currently operational setup, once using operational error estimates as reference (denoted as "operational experiment" thereafter),

https://doi.org/10.5194/egusphere-2025-6386
Preprint. Discussion started: 30 December 2025

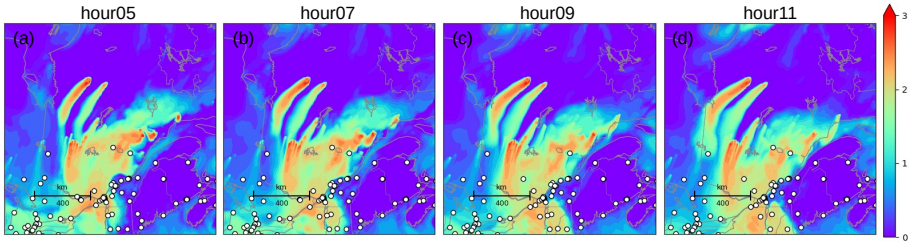

Figure 2. Background concentration fields on June 06, 2023 (logarithmic color code, colorbar labels represent exponent in $\log_{10}(\mu g\, m^{-3})$, hours in UTC). Assimilated surface observations are overplotted as white dots.

and once using parametric error forecasts provided by the GEM-MACH simulation (denoted as "parametric experiment" thereafter). Note that the OAv2 suite only performs hourly analyses with no feedback back into the next forecast. The OAv2 uses an lagged-time ensemble of past forecasts for the same time period to construct spatial error correlations. Spurious error correlations between distant locations are eliminated by applying a Schur product with a compact correlation function based on the Gaspari-Cohn fifth-order spline model (Gaspari and Cohn, 1999). The correlation length-scale of the Gaspari-Cohn model was deterimined by minimizing the analysis error variance evaluated by a cross-validation approach in Ménard and Deshaies-Jacques (2018b).

Using the new parametric error forecast as background error variances in the OAv2 assimilation induces three main differences to the operational formulation of background error variances: Firstly, the operational setup uses a bounded piecewise fit for the state-to-variance relation while the parametric setup uses a fully linear relation (compare Sec. 3.3). Secondly, this relation is applied to mean concentrations over a 2 month time period in the operational setup while being applied to instant concentration forecasts the parametric setup. Thirdly, the calculated error variances are directly used as background error estimates, thus providing purely statistical error estimates to the operational assimilation, while they only serve as input in the parametric error forecast providing highly case-dependent error estimates.

4.2 Error standard deviation forecasts

Figure 3 shows the surface fields of PM2.5 error standard deviation (also denoted as "error" thereafter) from the operational experiment and from the new parametric forecast. The parametric fields show significantly higher errors and gradients than the operational experiment, particularly in the regions affected by wildfires. This is because the operational error fields are estimated from long-term statistics and thus cannot account for case-specific uncertainties, particularly from wildfires (Fig. 3a-d). In contrast, the explicit consideration of emission uncertainties in the parametric forecast induces major error sources at the remote wildfire hotspots in central Quebec (Fig. 3e-h). Once emitted, the errors are propagated by advection and vertical diffusion, similar to the dynamics of the state concentrations (compare Sec. 2). Consequently, the extension of the error plumes and their propagation southwards to urban areas is qualitatively similar to the concentration fields (compare Fig. 2).

https://doi.org/10.5194/egusphere-2025-6386
Preprint. Discussion started: 30 December 2025

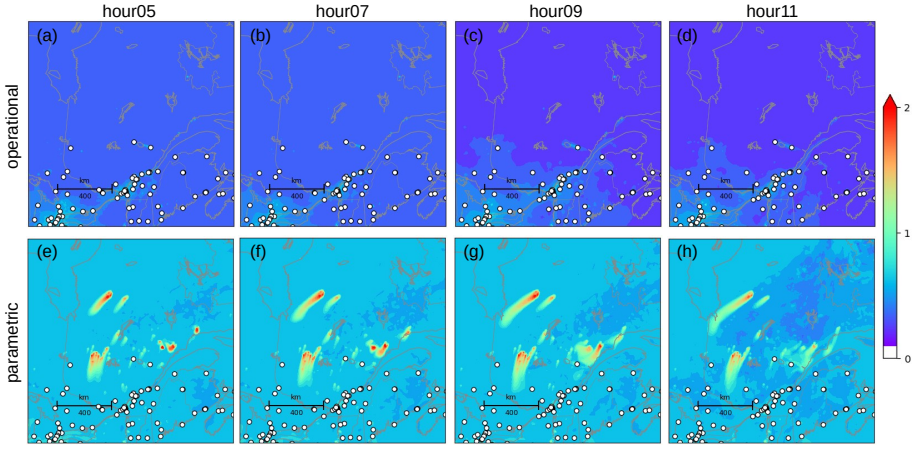

Figure 3. Background error standard deviations fields on June 06, 2023 (logarithmic color code, colorbar labels represent exponent in $\log_{10}(\mu g\,m^{-3})$, hours in UTC) from operational setup (a-d) and parametric forecast with L_ξ^z=6 model layers (e-h). Assimilated surface observations are overplotted as white dots.

Nevertheless, there are conceptual differences between the error field from the parametric forecast and the concentration forecast which are of high importance. Firstly, the error forecast does not include modifications due to processes like area emissions, chemical conversions and deposition (compare Sec. 2). Most significantly is the neglection of area emissions in the southern part including the urban areas of Montreal and Toronto. In these areas, the parametric errors are more similar to the operational error fields.

Secondly, the forecasted errors are reduced by the additional correlation term in the diffusion equation (compare Sec. 2.2). This term acts continuously on the error field reducing emission-related errors during their dispersion from sources to other regions. Consequently, the plumes of errors due to uncertain wildfire emissions vanish more quickly than the wildfire plumes in the concentration fields in Fig. 2. It can be seen from Eq. (12) that the strength of the correlation term is determined by the vertical error correlation length. A comparison for different vertical error correlation lengths in Apx. C shows that the impact on error standard deviation forecasts is stronger for shorter vertical error standard deviations.

It is important to note that the qualitative similarity of the error and state concentration forecast fields remains throughout the forecast period only because no analysis is feed back into the subsequent forecast in this simplified case study. In the analysis step, the change of state and error standard deviation due to assimilation of observations differ considerably. While the analysis state is a weighted linear combination between background and observation state, the analysis error standard deviation is always smaller than both, background and observation errors. Thus, the state and error forecasts differ more prominently as soon as any observation is assimilated in the system (see e.g. Voshtani et al., 2022, for an example).

https://doi.org/10.5194/egusphere-2025-6386
Preprint. Discussion started: 30 December 2025

4.3 Analysis Increments

Figure 4 shows analysis increments for surface PM2.5 from assimilating hourly surface observations into the operational experiment and the new parametric experiment. Generally, analysis increments vary significantly over time in both experiments, especially in the wildfire regions in central Quebec (central and northern part of the study domain) where the observation network is coarse. Note that the no-feedback setup in this study induces that each analysis increment is independent from the previous analyses the hours before, thus opposite corrections of wildfire plumes over time indicate highly variable forecast errors in opposite direction rather than balancing of previous analysis increments.

In the urban areas (southern part of the study domain), the new parametric experiments shows very similar analysis increments compared to the operational experiment w.r.t. both, spatial distribution and strength. A distinct area of strongly negative increments is moving from Ottawa south-eastward across the US border towards Boston and New York City. A comparison to the state forecast of the day before (not shown) indicates an overestimation of old wildfire plume concentrations which is spatio-temporally consistently captured by the urban observation network. The similarity between the two experiments can be attributed to their comparable error standard deviation fields (compare Fig. 3) in combination with good observation coverage in the urban areas leading to low impact of the parametric formulation.

In contrast, the parametric experiment shows considerably large increments in the northern remote areas along the wildfire plumes throughout the simulation period that cannot be found in the operational experiment. The strongly enhanced errors predicted by the parametric forecast along the plumes (compare Fig. 3e-h) induce exceptional spatial spreading of distant observation signals specifically to these locations. Consequently, analysis increments locally exceed values of $80\,\mu g\,m^{-3}$ even in the two large northern plumes which are about 400 km away from the nearest observation stations.

It is important to note that the two experiments only differ in their background error standard deviations, not in horizontal error correlation. The spreading of observation signals in the assimilation system is determined by the background error covariance matrix whose off-diagonal covariances are a product of background correlations between the two locations and their background error standard deviations. Thus, the large error standard deviations within the wildfire plumes in the parametric experiment enable significant increments even from weakly correlated observations.

Due to its large error estimates along the wildfire plumes, the parametric formulation induces analysis increments that are explicitly aligned with the forecasted plumes. In the remote wildfire areas with low observation coverage, increments are often attributed commonly to all surrounding plumes within a large region. For example, the two large northern plumes and the plumes close to the Saguenay Fjord are often commonly constraint by the two observations at the Fjord. However in some cases, the parametric experiment is still able to distinguish between individual plumes if different nearby observations indicate contradicting signals. When the observation constraint is strong enough, even strong opposite increments within a single plume can be found in the parametric experiment. Most prominently, the group of wildfire plumes in the western center of the study area (west of Gouin Reservoir) has strong local increments with opposite signs at 05 UTC.

https://doi.org/10.5194/egusphere-2025-6386
Preprint. Discussion started: 30 December 2025

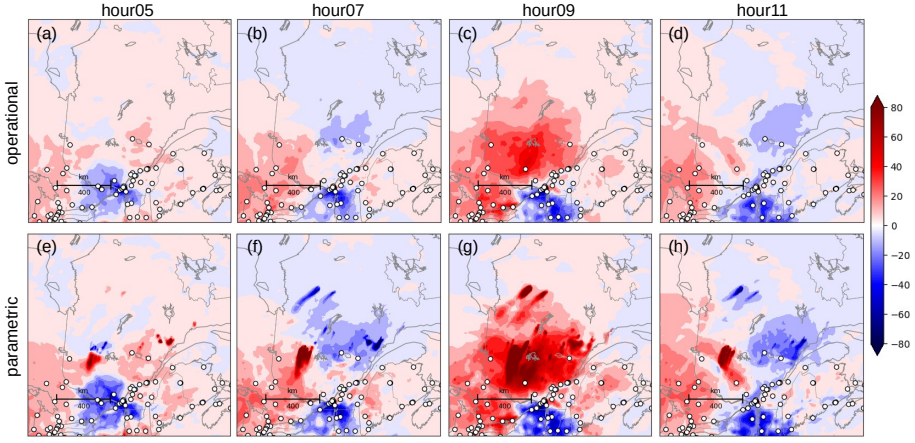

Figure 4. Analysis increments on June 06, 2023 (linear color code, colorbar labels give analysis-background increments in $\mu g\ m^{-3}$, hours in UTC) from operational setup (a-d) and parametric forecast with L_{ξ}^{z}=6 model layers (e-h). Assimilated surface observations are overplotted as white dots.

Note that the selection of vertical error correlation length also impacts the analysis increments as discussed in Apx. C. However, the comparison shows that the general properties of the parametric experiment described here remain applicable as long as vertical error correlation lengths stays within reasonable ranges.

5 Discussion and Conclusions

This study provides a simple parametric Kalman Filter (PKF) specifically tailored to the requirements of operational air quality data assimilation under highly uncertain emissions like wildfire smoke events. Operational smoke assimilation systems require fast, yet accurate error estimations which are able to represent the highly case-dependent, large and spatio-temporally variable uncertainties. While ensemble approaches have been demonstrated their suitability to capture such complex case-dependent uncertainties, their high computational costs are a major limitation especially in operational systems. Here, the potential of the PKF is exploited as an alternative approach in which the main error parameters are explicitly handled in the assimilation system. This study focuses on the forecast step of the PKF evolving error standard deviations in the operational air quality model GEM-MACH. This includes the following three steps: 1) theoretical derivation and investigation of forecast dynamics specific to the requirements of near-surface air quality applications under uncertain emissions, 2) implementation into the GEM-MACH modeling system, 3) application and evaluation of surface PM2.5 in eastern Canada during a wildfire case study in July 2023.

The first step requires the selection of important processes to be considered in the forecast of error parameters which is especially critical given the operational needs and limitations. The selection of advection, vertical diffusion and point emissions is made upon the principle "as few as possible, as many as necessary" to ensure fast, yet accurate error estimates for near-surface air quality applications. Parametric diffusion and emission processes are considered in a state-of-the-science atmospheric model

https://doi.org/10.5194/egusphere-2025-6386
Preprint. Discussion started: 30 December 2025

for the first time in this study. It turned out that error standard deviation is a more suitable parameter than variance because of multiple advantages that range from unit equivalence to simpler forecast equations which increase numerical accuracy and facilitate process-understanding (compare Sec. 2).

Although these two processes are critical for accurate error forecasts in air quality, they are highly sensitive to other error parameters. Is is shown that point emissions only change error parameters if the emissions are considered to be uncertain. Then, the increase of state error standard deviation is directly given by the related emission error standard deviation which thus significantly impacts the error forecast, especially for highly uncertain wildfire emissions. The change of error standard deviation or variance due to diffusion is shown to be sensitive to the respective error correlations (compare Apx. B2 and C). In this study, the vertical error correlation length is selected in a rather simple way to retain low computational demands and a decent amount of modifications in the forecast model. More sophisticated formulations will be investigated in future.

In the second step, the implementation into the GEM-MACH modeling system, the simpler forecast equation of error standard deviation becomes also advantageous because it only requires minor modifications in the forecast model (compare Sec. 3). In this study, point emissions of error variances are assumed to be proportional to local state emissions. Although this proportionality is consistent with the definitions of initial and boundary conditions (emission-to-concentration consistency), it is a highly simplified assumption of emission error behavior. Generally, each step including detection, quantification and distribution of emissions may have itself complex error sources that are not considered in this study. The current approach does also not account for forecast uncertainties of emission estimates of existing fires and their dynamics as well as uncertainties due to potential onset of new fires. Thus, the presented formulation only serves as first simple approach with focus on computational efficiency with large potential for future improvements.

For initial- and boundary conditions of error standard deviation, a simple linear state-to-variance relation is used to ensure emission-to-concentration consistency between uncertainties originating from uncertain emissions before and within the simulation period. Theoretically, this consistency would also hold in space, i.e. between emission uncertainties inside and outside of the forecast domain, but only if the related state input fields are consistent. In the current regional GEM-MACH, initial conditions are defined case-specific from the previous forecast, while monthly climatologies are used for lateral boundary conditions. Certainly, climatological boundary conditions are expected to have significantly larger uncertainties than case-specific initial conditions, even when - or exactly because - they have smaller concentrations. This inconsistency is not accounted for in the current setup, and thus boundary conditions for error fields are likely to underestimate true uncertainties. However, lateral boundary conditions play a minor role in the high-emission case presented here because state concentrations and their uncertainties are highly dominated by emissions and plume transport within the selected domain (see also Vogel et al., 2026). Ongoing developments of a global GEM-MACH would enable consistent input fields for state- as well as error fields.

The results from the wildfire case study demonstrate some important properties of the PKF for operational air quality. Firstly, the forecast of PM2.5 error standard deviation in GEM-MACH shows the suitability of parametric error forecasts in operational air quality systems. The application to wildfire smoke plumes demonstrates its ability to generate highly case-specific and anisotropic error fields at very low computational costs. Moreover, the error forecast results enable explicit investigation of the downstream propagation of errors due to highly uncertain emission sources. Secondly, the large spatio-temporal variability of

https://doi.org/10.5194/egusphere-2025-6386
Preprint. Discussion started: 30 December 2025

the PKF-based analysis increments show its ability of case and flow-dependent corrections. For low observation coverage close to the remote wildfire hotspots, the large background errors within the plumes enable specific spreading of distant observation information to these uncertain areas.

It is important to note that these significant increments far away from observations are only induced by large forecasted error standard deviations, not exaggerated background error correlations (see Sec. 4.3). In turn, this specific information spearing also means that corrections of remote wildfire plumes are highly determined by a few distant observations, each having significant influence on both, strength and shape on the corrections. This makes the PKF-based assimilation results more sensitive to individual observation information, while making improved use of the sparse observation network in this case study. For increased observation coverage, the PKF error estimates allow for more local corrections with possibly opposite increments within individual plumes, while keeping the consistency within a plume if confirmed by the observations. Thus, even the highly simplified PKF formulation used here enables highly specific and efficient use of the information content provided by sparse observation networks.

Although the error forecast model presented here was developed for wildfire smoke applications, it is generally applicable to other air quality events with highly uncertain emissions. Moreover, the implementation allows for a straight-forward extension to error standard deviation fields of multiple species in the model. This would however require some investigation concerning the validity of selected processes and potential cross-species correlations (see Perrot et al., 2023). Future work will first of all focus on a comprehensive validation of the analysis and its feedback back into the next forecast to enable full assimilation cycling for air quality when it is available in the GEM-MACH model. The general technical implementation of a full assimilation cycling in GEM-MACH is currently a development priority for research as well as operational purposes. The parametric from of an assimilation cycle also requires the analysis equation for the error parameters that will serve as initial conditions for the next error forecast. This parametric cycling is expected to show more clearly its benefits in terms of improved forecasts as well as understanding of error dynamics throughout multiple forecast-analysis cycles.

Concerning the forecast of error standard deviation of PM2.5, there are multiple potential improvements. These include for example improved formulations of error parameters like vertical error correlations and emission errors, the consideration of other uncertainties like wind, and the inclusion of other processes like area emissions, chemical conversions or deposition. The latter will be investigated in detail in a follow-up study. In addition, horizontal diffusion is not considered in this study because the regional operational GEM-MACH configuration does not include horizontal diffusion of the tracer fields. This is based on the assumption that numerical diffusion dominates physical horizontal diffusion in the regional domain. From a theoretical perspective, this assumption would in turn imply that the errors are still reduced by horizontal diffusion, even if the diffusion is caused by numerics rather than an explicit dynamical process. The consideration of related errors would require a considerably different derivation because it purely originates from the specific diffusion scheme in the model rather than the underlying partial differential equations (PDEs). Theoretical studies e.g. by Pannekoucke et al. (2021); Ménard et al. (2021); Gilpin et al. (2025) discuss inaccuracies in parametric error propagation due to discrete dynamics. For simplification, the current formulation only relates to uncertainties in the PDEs and thus implicitly assumes that the discrete numerical schemes are accurate.

https://doi.org/10.5194/egusphere-2025-6386
Preprint. Discussion started: 30 December 2025

Code and data availability. The developed GEM-MACH code and data produced in this study will be made available on Zenodo soon (before final publication). Until then, it is available from the authors.

Appendix A: Derivation of error dynamics

Numbers in brackets about equal signs indicate equation numbers used in this equation.

A1 Advection-diffusion-emission equation for errors

Let $\xi^t(\mathbf{x},t)$ be the true state of a passive tracer field propagated by an advection-diffusion-emission equation:

$$\partial_t \xi^t(\mathbf{x},t) = -\mathbf{u}(\mathbf{x},t)\cdot\nabla\xi^t(\mathbf{x},t) + \nabla\Big(\boldsymbol{\kappa}(\mathbf{x},t)\cdot\nabla\xi^t(\mathbf{x},t)\Big) + E^t(\mathbf{x},t) \tag{A1}$$

with true wind vector field $\mathbf{u}(\mathbf{x},t)$, diffusion tensor field $\boldsymbol{\kappa}(\mathbf{x},t)$ and emission field $E^t(\mathbf{x},t)$.

Assuming an accurate dynamical model with true diffusion coefficient and wind fields, the estimated tracer field $\xi(\mathbf{x},t)$ is propagated by the same advection equation:

$$\partial_t \xi(\mathbf{x},t) = -\mathbf{u}(\mathbf{x},t)\cdot\nabla\xi(\mathbf{x},t) + \nabla\Big(\boldsymbol{\kappa}(\mathbf{x},t)\cdot\nabla\xi(\mathbf{x},t)\Big) + E(\mathbf{x},t) \tag{A2}$$

with $E(\mathbf{x},t)$ the estimated emission field in the model.

Further, assuming unbiased random errors for states $\epsilon_\xi(\mathbf{x},t)$ and emissions $\epsilon_E(\mathbf{x},t)$:

$$\epsilon_\xi(\mathbf{x},t) := \xi(\mathbf{x},t) - \xi^t(\mathbf{x},t) \tag{A3}$$

$$\epsilon_E(\mathbf{x},t) := E(\mathbf{x},t) - E^t(\mathbf{x},t) \tag{A4}$$

the propagation of state error $\epsilon_\xi(\mathbf{x},t)$ due to advection-diffusion-emission processes is given as follows:

$$\begin{aligned}
\partial_t\epsilon_\xi(\mathbf{x},t) &\overset{(A3)}{=} \partial_t\Big(\xi^t(\mathbf{x},t) - \xi(\mathbf{x},t)\Big) = \partial_t\xi^t(\mathbf{x},t) - \partial_t\xi(\mathbf{x},t) \\
&\overset{(A1),(A2)}{=} \Big[-\mathbf{u}(\mathbf{x},t)\cdot\nabla\xi^t(\mathbf{x},t) + \nabla\Big(\boldsymbol{\kappa}(\mathbf{x},t)\cdot\nabla\xi^t(\mathbf{x},t)\Big) + E(\mathbf{x},t)\Big] - \Big[-\mathbf{u}(\mathbf{x},t)\cdot\nabla\xi(\mathbf{x},t) + \nabla\Big(\boldsymbol{\kappa}(\mathbf{x},t)\cdot\nabla\xi(\mathbf{x},t)\Big) + E(\mathbf{x},t)\Big] \\
&= -\mathbf{u}(\mathbf{x},t)\cdot\nabla\Big(\xi^t(\mathbf{x},t) - \xi(\mathbf{x},t)\Big) + \nabla\Big(\boldsymbol{\kappa}(\mathbf{x},t)\cdot\nabla\left(\xi^t(\mathbf{x},t) - \xi(\mathbf{x},t)\right)\Big) + E^t(\mathbf{x},t) - E(\mathbf{x},t) \\
&\overset{(A4)}{=} -\mathbf{u}(\mathbf{x},t)\cdot\nabla\epsilon_\xi(\mathbf{x},t) + \nabla\Big(\boldsymbol{\kappa}(\mathbf{x},t)\cdot\nabla\epsilon_\xi(\mathbf{x},t)\Big) + \epsilon_E(\mathbf{x},t)
\end{aligned} \tag{A5}$$

Thus, the state error is propagated with the same linear forecast dynamics as the state itself. A more general derivation and discussion of the error propagation equations without emissions can be found in Pannekoucke et al. (2018), their Sec.3.1.

https://doi.org/10.5194/egusphere-2025-6386
Preprint. Discussion started: 30 December 2025

A2 General propagation of error variance and standard deviation

Given the definitions of error variance and standard deviation in Eq. (3) and Eq. (4), respectively, the general propagation of these two error parameters can be formulated as follows:

$$\partial_t V_\xi(\mathbf{x},t) \overset{(3)}{=} \partial_t \overline{\Big(\epsilon_\xi(\mathbf{x},t)\Big)^2} = 2\,\overline{\epsilon_\xi(\mathbf{x},t)\cdot\partial_t\epsilon_\xi(\mathbf{x},t)} \tag{A6}$$

$$\partial_t \sigma_\xi(\mathbf{x},t) \overset{(4)}{=} \partial_t \sqrt{V_\xi(\mathbf{x},t)} = \frac{1}{2\sqrt{V_\xi(\mathbf{x},t)}}\cdot\partial_t V_\xi(\mathbf{x},t) \overset{(A6)}{=} \frac{1}{\sigma_\xi(\mathbf{x},t)}\cdot\overline{\epsilon_\xi(\mathbf{x},t)\cdot\partial_t\epsilon_\xi(\mathbf{x},t)} \tag{A7}$$

A3 3D advection equation for error variance and standard deviation

3D advection equation for forecast error $\epsilon_\xi(\mathbf{x},t)$ into directions $\mathbf{x} := [x,y,z]^T$:

$$\partial_t\epsilon_\xi(\mathbf{x},t)\Big|_{\text{adv}} \overset{(A5)}{=} -\mathbf{u}(\mathbf{x},t)\cdot\nabla\epsilon_\xi(\mathbf{x},t) \tag{A8}$$

Propagation of forecast error variance $V_\xi(\mathbf{x},t)$ by pure advection:

$$\partial_t V_\xi(\mathbf{x},t)\Big|_{\text{adv}} \overset{(A6)}{=} 2\,\overline{\epsilon_\xi(\mathbf{x},t)\cdot\partial_t\epsilon_\xi(\mathbf{x},t)\Big|_{\text{adv}}} \overset{(A8)}{=} -2\,\mathbf{u}(\mathbf{x},t)\cdot\overline{\epsilon_\xi(\mathbf{x},t)\cdot\nabla\epsilon_\xi(\mathbf{x},t)} \tag{A9}$$

Using:

$$\nabla V_\xi(\mathbf{x},t) := \nabla\overline{\Big(\epsilon_\xi(\mathbf{x},t)\Big)^2} = 2\,\overline{\epsilon_\xi(\mathbf{x},t)\cdot\nabla\epsilon_\xi(\mathbf{x},t)} \tag{A10}$$

Gives:

$$\overset{(A9)}{\Longrightarrow} \quad \partial_t V_\xi(\mathbf{x},t)\Big|_{\text{adv}} \overset{(A10)}{=} -\,\mathbf{u}(\mathbf{x},t)\cdot\nabla V_\xi(\mathbf{x},t) \tag{A11}$$

Similarly, the propagation of forecast error standard deviation $\sigma_\xi(\mathbf{x},t)$ by pure advection:

$$\partial_t\sigma_\xi(\mathbf{x},t)\Big|_{\text{vdiff}} \overset{(A7)}{=} \frac{1}{\sigma_\xi(\mathbf{x},t)}\cdot\overline{\epsilon_\xi(\mathbf{x},t)\cdot\partial_t\epsilon_\xi(\mathbf{x},t)\Big|_{\text{vdiff}}} \overset{(A8)}{=} -\frac{1}{\sigma_\xi(\mathbf{x},t)}\cdot\mathbf{u}(\mathbf{x},t)\cdot\overline{\epsilon_\xi(\mathbf{x},t)\cdot\nabla\epsilon_\xi(\mathbf{x},t)} \tag{A12}$$

Using:

$$\nabla\sigma_\xi(\mathbf{x},t) := \nabla\sqrt{V_\xi(\mathbf{x},t)} = \frac{1}{2\sqrt{V_\xi(\mathbf{x},t)}}\nabla V_\xi(\mathbf{x},t)\cdot \overset{(A10)}{=} \cancel{2}\,\frac{1}{\cancel{2}\,\sigma_\xi(\mathbf{x},t)}\cdot\overline{\epsilon_\xi(\mathbf{x},t)\cdot\nabla\epsilon_\xi(\mathbf{x},t)} \tag{A13}$$

Gives:

$$\overset{(A12)}{\Longrightarrow} \quad \partial_t\sigma_\xi(\mathbf{x},t)\Big|_{\text{adv}} \overset{(A13)}{=} -\,\mathbf{u}(\mathbf{x},t)\cdot\nabla\sigma_\xi(\mathbf{x},t) \tag{A14}$$

Note that these propagation equations due to advection were also derived by Pannekoucke et al. (2018), their Sec.3.2.2.

https://doi.org/10.5194/egusphere-2025-6386
Preprint. Discussion started: 30 December 2025

A4 1D diffusion equation for error variance

1D diffusion equation for random error $\epsilon_\xi(\mathbf{x},t)$ into direction z:

$$\partial_t \epsilon_\xi(\mathbf{x},t)\Big|_{\text{vdiff}} \overset{(A5)}{=} \partial_z\Big(\kappa^z(\mathbf{x},t)\cdot\partial_z\epsilon_\xi(\mathbf{x},t)\Big) \tag{A15}$$

with $\kappa^z(\mathbf{x},t)$ the vertical diffusion coefficient.

Propagation of forecast error variance $V_\xi(\mathbf{x},t)$ by pure diffusion:

$$\begin{aligned}\partial_t V_\xi(\mathbf{x},t)\Big|_{\text{vdiff}} &\overset{(A6)}{=} 2\,\overline{\epsilon_\xi(\mathbf{x},t)\cdot\partial_t\epsilon_\xi(\mathbf{x},t)\Big|_{\text{vdiff}}} \overset{(A15)}{=} 2\,\overline{\epsilon_\xi(\mathbf{x},t)\cdot\partial_z\Big(\kappa^z(\mathbf{x},t)\cdot\partial_z\epsilon_\xi(\mathbf{x},t)\Big)} \\ &= 2\,\partial_z\kappa^z(\mathbf{x},t)\cdot\overline{\epsilon_\xi(\mathbf{x},t)\cdot\partial_z\epsilon_\xi(\mathbf{x},t)} + 2\,\kappa^z(\mathbf{x},t)\cdot\overline{\epsilon_\xi(\mathbf{x},t)\cdot\partial_z^2\epsilon_\xi(\mathbf{x},t)}\end{aligned} \tag{A16}$$

Using:

$$\partial_z V_\xi(\mathbf{x},t) := \partial_z\left[\overline{\Big(\epsilon_\xi(\mathbf{x},t)\Big)^2}\right] = 2\,\overline{\epsilon_\xi(\mathbf{x},t)\cdot\partial_z\epsilon_\xi(\mathbf{x},t)} \tag{A17a}$$

$$\partial_z^2 V_\xi(\mathbf{x},t) := \partial_z^2\left[\overline{\Big(\epsilon_\xi(\mathbf{x},t)\Big)^2}\right] \overset{(A17a)}{=} 2\,\partial_z\Big(\overline{\epsilon_\xi(\mathbf{x},t)\cdot\partial_z\epsilon_\xi(\mathbf{x},t)}\Big) = 2\,\overline{\Big(\partial_z\epsilon_\xi(\mathbf{x},t)\Big)^2} + 2\,\overline{\epsilon_\xi(\mathbf{x},t)\cdot\partial_z^2\epsilon_\xi(\mathbf{x},t)} \tag{A17b}$$

Defining normalized errors $\tilde{\epsilon}_\xi(\mathbf{x},t)$:

$$\tilde{\epsilon}_\xi(\mathbf{x},t) := \frac{\epsilon_\xi(\mathbf{x},t)}{\sigma_\xi(\mathbf{x},t)} \tag{A18}$$

with: $\overline{(\tilde{\epsilon}_\xi(\mathbf{x},t))^2} =: 1$ by definition, (A19a)

and: $\overline{\tilde{\epsilon}_\xi(\mathbf{x},t)\cdot\partial_z\tilde{\epsilon}_\xi(\mathbf{x},t)} = 0$ which follows directly e.g. from Eq. (A17a) or (A26a). (A19b)

and the definition of the 1D error correlation length into direction z:

$$L_\xi^z(\mathbf{x},t) := \left[\overline{\Big(\partial_z\tilde{\epsilon}_\xi(\mathbf{x},t)\Big)^2}\right]^{-\frac{1}{2}} \tag{A20}$$

Gives:

$$\begin{aligned}\overline{\Big(\partial_z\epsilon_\xi(\mathbf{x},t)\Big)^2} &\overset{(A18)}{=} \overline{\Big[\partial_z\Big(\tilde{\epsilon}_\xi(\mathbf{x},t)\cdot\sigma_\xi(\mathbf{x},t)\Big)\Big]^2} = \overline{\Big(\tilde{\epsilon}_\xi(\mathbf{x},t)\cdot\partial_z\sigma_\xi(\mathbf{x},t) + \partial_z\tilde{\epsilon}_\xi(\mathbf{x},t)\cdot\sigma_\xi(\mathbf{x},t)\Big)^2} \\ &= \overline{\Big(\tilde{\epsilon}_\xi(\mathbf{x},t)\Big)^2}\cdot\Big(\partial_z\sigma_\xi(\mathbf{x},t)\Big)^2 + 2\,\overline{\tilde{\epsilon}_\xi(\mathbf{x},t)\cdot\partial_z\tilde{\epsilon}_\xi(\mathbf{x},t)}\cdot\partial_z\sigma_\xi(\mathbf{x},t)\cdot\sigma_\xi(\mathbf{x},t) + \overline{\Big(\partial_z\tilde{\epsilon}_\xi(\mathbf{x},t)\Big)^2}\cdot\Big(\sigma_\xi(\mathbf{x},t)\Big)^2 \\ &\overset{(A19),(A20)}{=} \Big(\partial_z\sigma_\xi(\mathbf{x},t)\Big)^2 + \Big(L_\xi^z(\mathbf{x},t)\Big)^{-2}\cdot V_\xi(\mathbf{x},t)\end{aligned} \tag{A21}$$

And using:

$$\Big(\partial_z V_\xi(\mathbf{x},t)\Big)^2 := \Big[\partial_z\Big(\sigma_\xi(\mathbf{x},t)\Big)^2\Big]^2 = \Big(2\,\sigma_\xi(\mathbf{x},t)\cdot\partial_z\sigma_\xi(\mathbf{x},t)\Big)^2 = 4\,V_\xi(\mathbf{x},t)\cdot\Big(\partial_z\sigma_\xi(\mathbf{x},t)\Big)^2 \tag{A22}$$

https://doi.org/10.5194/egusphere-2025-6386
Preprint. Discussion started: 30 December 2025

Gives:

$$\overset{(A17b)}{\Longrightarrow} \quad \partial_z^2 V_\xi(\mathbf{x},t) \overset{(A21)}{=} 2\left(\partial_z \sigma_\xi(\mathbf{x},t)\right)^2 + 2\left(L_\xi^z(\mathbf{x},t)\right)^{-2} \cdot V_\xi(\mathbf{x},t) + 2\,\overline{\epsilon_\xi(\mathbf{x},t)\cdot\partial_z^2\epsilon_\xi(\mathbf{x},t)}$$
$$\overset{(A22)}{=} \frac{\left(\partial_z V_\xi(\mathbf{x},t)\right)^2}{2\,V_\xi(\mathbf{x},t)} + 2\left(L_\xi^z(\mathbf{x},t)\right)^{-2} \cdot V_\xi(\mathbf{x},t) + 2\,\overline{\epsilon_\xi(\mathbf{x},t)\cdot\partial_z^2\epsilon_\xi(\mathbf{x},t)} \tag{A23}$$

Which finally gives the propagation of error variance due to 1D diffusion:

$$\overset{(A16)}{\Longrightarrow} \quad \partial_t V_\xi(\mathbf{x},t)\Big|_{\text{vdiff}} \overset{(A17a),(A23)}{=} \partial_z\kappa^z(\mathbf{x},t)\cdot\partial_z V_\xi(\mathbf{x},t) + \kappa^z(\mathbf{x},t)\cdot\left[\partial_z^2 V_\xi(\mathbf{x},t) - \frac{\left(\partial_z V_\xi(\mathbf{x},t)\right)^2}{2\,V_\xi(\mathbf{x},t)} - 2\left(L_\xi^z(\mathbf{x},t)\right)^{-2}\cdot V_\xi(\mathbf{x},t)\right]$$
$$= \partial_z\left(\kappa^z(\mathbf{x},t)\cdot\partial_z V_\xi(\mathbf{x},t)\right) - \kappa^z(\mathbf{x},t)\cdot\frac{\left(\partial_z V_\xi(\mathbf{x},t)\right)^2}{2\,V_\xi(\mathbf{x},t)} - 2\,\kappa^z(\mathbf{x},t)\cdot\left(L_\xi^z(\mathbf{x},t)\right)^{-2}\cdot V_\xi(\mathbf{x},t)$$
$$\partial_t V_\xi(\mathbf{x},t)\Big|_{\text{vdiff}} = \partial_z\left(\kappa^z(\mathbf{x},t)\cdot\partial_z V_\xi(\mathbf{x},t)\right) - \kappa^z(\mathbf{x},t)\cdot V_\xi(\mathbf{x},t)\left[\left(\frac{\partial_z V_\xi(\mathbf{x},t)}{2\,V_\xi(\mathbf{x},t)}\right)^2 + 2\left(L_\xi^z(\mathbf{x},t)\right)^{-2}\right] \tag{A24}$$

Note that Pannekoucke et al. (2018) also derive this propagation equations for error variance due to diffusion, in their Sec.3.2.3, but using the error correlation tensor instead.

A5 1D diffusion equation for error standard deviation

Propagation of forecast error standard deviation $\sigma_\xi(\mathbf{x},t)$ by 1D diffusion into direction z:

$$\partial_t\sigma_\xi(\mathbf{x},t)\Big|_{\text{vdiff}} \overset{(A7)}{=} \frac{1}{\sigma_\xi(\mathbf{x},t)}\cdot\overline{\epsilon_\xi(\mathbf{x},t)\cdot\partial_t\epsilon_\xi(\mathbf{x},t)\Big|_{\text{vdiff}}} \overset{(A15)}{=} \frac{1}{\sigma_\xi(\mathbf{x},t)}\cdot\overline{\epsilon_\xi(\mathbf{x},t)\cdot\partial_z\left(\kappa^z(\mathbf{x},t)\cdot\partial_z\epsilon_\xi(\mathbf{x},t)\right)}$$
$$= \frac{1}{\sigma_\xi(\mathbf{x},t)}\cdot\partial_z\kappa^z(\mathbf{x},t)\cdot\overline{\epsilon_\xi(\mathbf{x},t)\cdot\partial_z\epsilon_\xi(\mathbf{x},t)} + \frac{1}{\sigma_\xi(\mathbf{x},t)}\cdot\kappa^z(\mathbf{x},t)\cdot\overline{\epsilon_\xi(\mathbf{x},t)\cdot\partial_z^2\epsilon_\xi(\mathbf{x},t)} \tag{A25}$$

Using:

$$\partial_z\sigma_\xi(\mathbf{x},t) = \frac{1}{2\,\sigma_\xi(\mathbf{x},t)}\cdot\partial_z\left(\sigma_\xi(\mathbf{x},t)\right)^2 = \frac{1}{2\,\sigma_\xi(\mathbf{x},t)}\partial_z V_\xi(\mathbf{x},t) \overset{(A17a)}{=} \frac{1}{\sigma_\xi(\mathbf{x},t)}\cdot\overline{\epsilon_\xi(\mathbf{x},t)\cdot\partial_z\epsilon_\xi(\mathbf{x},t)} \tag{A26a}$$

$$\partial_z^2\sigma_\xi(\mathbf{x},t) = \partial_z\left(\partial_z\sigma_\xi(\mathbf{x},t)\right) \overset{(A26a)}{=} \partial_z\left[\frac{1}{\sigma_\xi(\mathbf{x},t)}\cdot\overline{\epsilon_\xi(\mathbf{x},t)\cdot\partial_z\epsilon_\xi(\mathbf{x},t)}\right]$$
$$= \left(\partial_z\frac{1}{\sigma_\xi(\mathbf{x},t)}\right)\cdot\overline{\epsilon_\xi(\mathbf{x},t)\cdot\partial_z\epsilon_\xi(\mathbf{x},t)} + \frac{1}{\sigma_\xi(\mathbf{x},t)}\cdot\overline{\left(\partial_z\epsilon_\xi(\mathbf{x},t)\right)^2} + \frac{1}{\sigma_\xi(\mathbf{x},t)}\cdot\overline{\epsilon_\xi(\mathbf{x},t)\cdot\partial_z^2\epsilon_\xi(\mathbf{x},t)}$$
$$= -\frac{1}{\sigma_\xi(\mathbf{x},t)^2}\cdot\partial_z\sigma_\xi(\mathbf{x},t)\cdot\overline{\epsilon_\xi(\mathbf{x},t)\cdot\partial_z\epsilon_\xi(\mathbf{x},t)} + \frac{1}{\sigma_\xi(\mathbf{x},t)}\cdot\overline{\left(\partial_z\epsilon_\xi(\mathbf{x},t)\right)^2} + \frac{1}{\sigma_\xi(\mathbf{x},t)}\cdot\overline{\epsilon_\xi(\mathbf{x},t)\cdot\partial_z^2\epsilon_\xi(\mathbf{x},t)} \tag{A26b}$$

https://doi.org/10.5194/egusphere-2025-6386
Preprint. Discussion started: 30 December 2025

Gives:

$$\overset{(A25)}{\Longrightarrow} \quad \partial_t \sigma_\xi(\mathbf{x},t)\Big|_{\text{vdiff}} \overset{(A26b)}{=} \frac{1}{\sigma_\xi(\mathbf{x},t)} \cdot \partial_z \kappa^z(\mathbf{x},t) \cdot \overline{\epsilon_\xi(\mathbf{x},t) \cdot \partial_z \epsilon_\xi(\mathbf{x},t)}$$

$$+ \kappa^z(\mathbf{x},t) \cdot \left[\partial_z^2 \sigma_\xi(\mathbf{x},t) + \frac{1}{\sigma_\xi(\mathbf{x},t)^2} \cdot \partial_z \sigma_\xi(\mathbf{x},t) \cdot \overline{\epsilon_\xi(\mathbf{x},t) \cdot \partial_z \epsilon_\xi(\mathbf{x},t)} - \frac{1}{\sigma_\xi(\mathbf{x},t)} \cdot \overline{\left(\partial_z \epsilon_\xi(\mathbf{x},t)\right)^2} \right]$$

$$\overset{(A26a)}{=} \partial_z \kappa^z(\mathbf{x},t) \cdot \partial_z \sigma_\xi(\mathbf{x},t) + \kappa^z(\mathbf{x},t)\, \partial_z^2 \sigma_\xi(\mathbf{x},t) + \kappa^z(\mathbf{x},t) \cdot \frac{1}{\sigma_\xi(\mathbf{x},t)} \left(\partial_z \sigma_\xi(\mathbf{x},t)\right)^2$$

$$- \kappa^z(\mathbf{x},t) \cdot \frac{1}{\sigma_\xi(\mathbf{x},t)} \cdot \overline{\left(\partial_z \epsilon_\xi(\mathbf{x},t)\right)^2}$$

$$\overset{(A21)}{=} \partial_z \kappa^z(\mathbf{x},t) \cdot \partial_z \sigma_\xi(\mathbf{x},t) + \kappa^z(\mathbf{x},t) \cdot \partial_z^2 \sigma_\xi(\mathbf{x},t) + \kappa^z(\mathbf{x},t) \cdot \frac{1}{\sigma_\xi(\mathbf{x},t)} \cdot \cancel{\left(\partial_z \sigma_\xi(\mathbf{x},t)\right)^2}$$

$$- \kappa^z(\mathbf{x},t) \cdot \frac{1}{\sigma_\xi(\mathbf{x},t)} \left[\cancel{\left(\partial_z \sigma_\xi(\mathbf{x},t)\right)^2} + \left(L_\xi^z(\mathbf{x},t)\right)^{-2} \cdot \left(\sigma_\xi(\mathbf{x},t)\right)^2 \right]$$

$$= \partial_z \kappa^z(\mathbf{x},t) \cdot \partial_z \sigma_\xi(\mathbf{x},t) + \kappa^z(\mathbf{x},t) \cdot \partial_z^2 \sigma_\xi(\mathbf{x},t) - \kappa^z(\mathbf{x},t) \cdot \cancel{\frac{1}{\sigma_\xi(\mathbf{x},t)}} \cdot \left(L_\xi^z(\mathbf{x},t)\right)^{-2} \cdot \cancel{\left(\sigma_\xi(\mathbf{x},t)\right)^2}$$

$$= \partial_z \Big(\kappa^z(\mathbf{x},t) \cdot \partial_z \sigma_\xi(\mathbf{x},t) \Big) - \kappa^z(\mathbf{x},t) \cdot \left(L_\xi^z(\mathbf{x},t)\right)^{-2} \cdot \sigma_\xi(\mathbf{x},t) \tag{A27}$$

A6 Point emission equation for error variance and standard deviation

The change of state concentrations due to point emissions (=locally added emission amount per timestep and gridbox) of each species is given by:

$$\partial_t \xi(\mathbf{x},t)\Big|_{\text{p.emis}} \overset{(1)}{=} E(\mathbf{x},t) \tag{A28}$$

Then the error due to uncertainties in the prescribed emission field $E(\mathbf{x},t)$ is given by its deviation from the true emission field $E^t(\mathbf{x},t)$:

$$\partial_t \epsilon_\xi(\mathbf{x},t)\Big|_{\text{p.emis}} \overset{(2)}{=} \partial_t \Big[\xi(\mathbf{x},t) - \xi^t(\mathbf{x},t)\Big]_{\text{p.emis}} = \partial_t \xi(\mathbf{x},t)\Big|_{\text{p.emis}} - \partial_t \xi^t(\mathbf{x},t)\Big|_{\text{p.emis}} \overset{(A28)}{=} E(\mathbf{x},t) - E^t(\mathbf{x},t) \quad := \epsilon_E(\mathbf{x},t) \tag{A29}$$

with $\epsilon_E(\mathbf{x},t)$ the error in emission field of that species.

With this, the change of concentration error variance due to uncertain emissions becomes:

$$\partial_t V_\xi(\mathbf{x},t)\Big|_{\text{adv}} \overset{(A6)}{=} 2\, \overline{\epsilon_\xi(\mathbf{x},t) \cdot \partial_t \epsilon_\xi(\mathbf{x},t)\Big|_{\text{adv}}} \overset{(A29)}{=} 2\, \overline{\epsilon_\xi(\mathbf{x},t) \cdot \epsilon_E(\mathbf{x},t)} \tag{A30}$$

Defining normalized errors of concentration and emissions:

$$\tilde{\epsilon}_\xi(\mathbf{x},t) := \frac{\epsilon_\xi(\mathbf{x},t)}{\sigma_\xi(\mathbf{x},t)} \tag{A31a}$$

$$\tilde{\epsilon}_E(\mathbf{x},t) := \frac{\epsilon_E(\mathbf{x},t)}{\sigma_E(\mathbf{x},t)} \tag{A31b}$$

https://doi.org/10.5194/egusphere-2025-6386
Preprint. Discussion started: 30 December 2025

Gives:

$$\overset{(A30)}{\Longrightarrow} \quad \partial_t V_\xi(\mathbf{x},t)\Big|_{\text{p.emis}} \overset{(A31)}{=} 2\,\sigma_\xi(\mathbf{x},t)\cdot\sigma_E(\mathbf{x},t)\cdot\overline{\tilde{\epsilon}_\xi(\mathbf{x},t)\cdot\tilde{\epsilon}_E(\mathbf{x},t)} \tag{A32}$$

Where $\overline{\tilde{\epsilon}_\xi(\mathbf{x},t)\cdot\tilde{\epsilon}_E(\mathbf{x},t)}$ is the correlation between concentration- and emission errors, thus the concentration error standard deviation is increasing with the parallel component of the emission error to the concentration error (i.e. maximal increase if emission error is in the same direction as concentration error, but no change if concentration errors are completely independent from emission errors).

Assuming concentration errors at emission locations to be highly correlated to local emission errors $\overline{\tilde{\epsilon}_\xi(\mathbf{x},t)\cdot\tilde{\epsilon}_E(\mathbf{x},t)}\approx 1$ leads to the following approximation:

$$\overset{(A32)}{\Longrightarrow} \quad \partial_t V_\xi(\mathbf{x},t)\Big|_{\text{p.emis}} \approx 2\,\sigma_\xi(\mathbf{x},t)\cdot\sigma_E(\mathbf{x},t) \tag{A33}$$

Similarly, the change of concentration error standard deviation due to uncertain emissions is given by:

$$\partial_t\sigma_\xi(\mathbf{x},t)\Big|_{\text{p.emis}} \overset{(A7)}{=} \frac{1}{\sigma_\xi(\mathbf{x},t)}\cdot\overline{\epsilon_\xi(\mathbf{x},t)\cdot\partial_t\epsilon_\xi(\mathbf{x},t)\Big|_{\text{p.emis}}} \overset{(A29)}{=} \frac{1}{\sigma_\xi(\mathbf{x},t)}\cdot\overline{\epsilon_\xi(\mathbf{x},t)\cdot\epsilon_E(\mathbf{x},t)} \tag{A34}$$

Again, using normalized errors gives:

$$\overset{(A34)}{\Longrightarrow} \quad \partial_t\sigma_\xi(\mathbf{x},t)\Big|_{\text{p.emis}} \overset{(A31)}{=} \sigma_E(\mathbf{x},t)\cdot\overline{\tilde{\epsilon}_\xi(\mathbf{x},t)\cdot\tilde{\epsilon}_E(\mathbf{x},t)} \tag{A35}$$

And assuming highly correlated errors leads to the approximation:

$$\overset{(A35)}{\Longrightarrow} \quad \partial_t\sigma_\xi(\mathbf{x},t)\Big|_{\text{p.emis}} \approx \sigma_E(\mathbf{x},t) \tag{A36}$$

Thus for point emissions-only, the concentration error standard deviation increases linearly with the emission error standard deviation:

$$\overset{(A36)}{\Longrightarrow} \quad \sigma_\xi(\mathbf{x},t)\Big|_{\text{p.emis}} \approx \sigma_\xi(\mathbf{x},t_0) + \sigma_E(\mathbf{x},t)\cdot\Delta t \tag{A37}$$

with $\sigma_\xi(\mathbf{x},t_0)$ the initial condition of concentration error standard deviation for timestep $\Delta t := t - t_0$.

For comparison, the prognostic equation for concentration error variance in Eq. (A33) includes the concentration error standard deviation on the right-hand-side, which results in a quadratic increase over time:

$$\begin{aligned}\overset{(A33)}{\Longrightarrow} \quad V_\xi(\mathbf{x},t)\Big|_{\text{p.emis}} &:= \left[\sigma_\xi(\mathbf{x},t)\Big|_{\text{p.emis}}\right]^2 \overset{(A37)}{\approx} \left[\sigma_\xi(\mathbf{x},t_0) + \sigma_E(\mathbf{x},t)\,\Delta t\right]^2 \\ &= V_\xi(\mathbf{x},t_0) + 2\,\sigma_\xi(\mathbf{x},t_0)\,\sigma_E(\mathbf{x},t)\,\Delta t + V_E(\mathbf{x},t)\,\left[\Delta t\right]^2\end{aligned} \tag{A38}$$

with $V_\xi(\mathbf{x},t_0)$ the initial condition of concentration error variance.

https://doi.org/10.5194/egusphere-2025-6386
Preprint. Discussion started: 30 December 2025

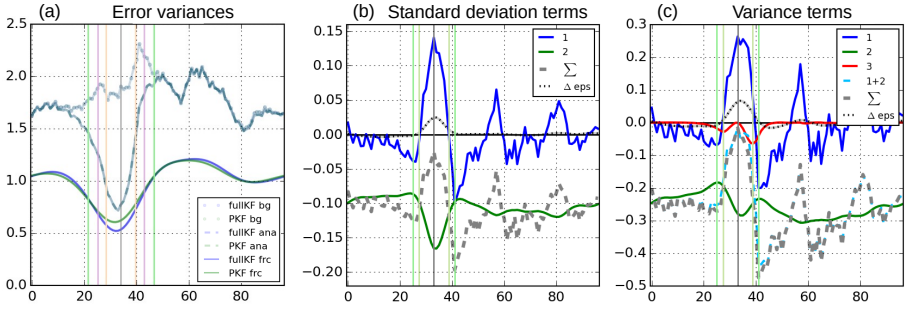

Figure B1. Comparison of individual terms (solid colored lines) in idealized 1D experiment for diffusion calculated from the variance form in Eq. (11) (b) and from the standard deviation form in Eq. (12) (c), respectively, from the first diffusion timestep. Dashed lines indicate the sum over terms 1+2 (light blue) and all terms (gray), respectively. The residual difference to the full KF is given as grey-black dotted line. Vertical lines indicate the observation location (gray), and related error correlation lengths for background (pink), analysis before diffusion (orange), forecast before current diffusion timestep (light green), and after diffusion (green). Note the different units of the vertical axis referring to the change of error variance (b) and standard deviation (c), respectively. Figure (a): variance fields of background (dotted), analysis (dashed) and diffusion forecast (solid) for the full KF (blue) and PKF using the standard deviation form (green), respectively.

Appendix B: Idealized experiments for 1D diffusion

B1 Comparison of variance- and standard deviation-form

Figure B1 visualizes the individual terms contributing to the change of error variance and standard deviation due to diffusion in an idealized 1D experiment. Starting from an artificial background variance field (Fig. B1a), a single observation is assimilated at gridpoint 34. Afterwards strong diffusion was considered as forecast step to clearly show the impact of the individual terms for each formulation (Fig. B1b,c). For both formulations, the smoothing effect of the standard diffusion term (term 1) and the overall reducing effect of the correlation term (term 2) are clearly visible (compare Sec. 2.2). However, the variance form has an additional term (gradient term, term 3) which reduces error variance at strong spatial gradients (compare Eq. (11)). Because the two formulations are mathematically identical, the first two terms are locally larger in the variance form compared to the standard deviation form in which the impact of the gradient term (term 3) is implicitly accounted for in the other two terms. Consequently, the strength and shape of the first two terms differ between the two formulations.

In terms of interpretability, the standard deviation form shows more clearly the increased reduction by the correlation term (term 2) at locations with reduced error correlations around the observation (compare Eq. (12)). A comparison of the net residual of the parametric formulations to the full Kalman Filter shows that the standard deviation form is more accurate which can be attributed to additional numerical uncertainties in the gradient term of the variance form. For a more detailed description of the remaining residuals see Apx. B2.

https://doi.org/10.5194/egusphere-2025-6386
Preprint. Discussion started: 30 December 2025

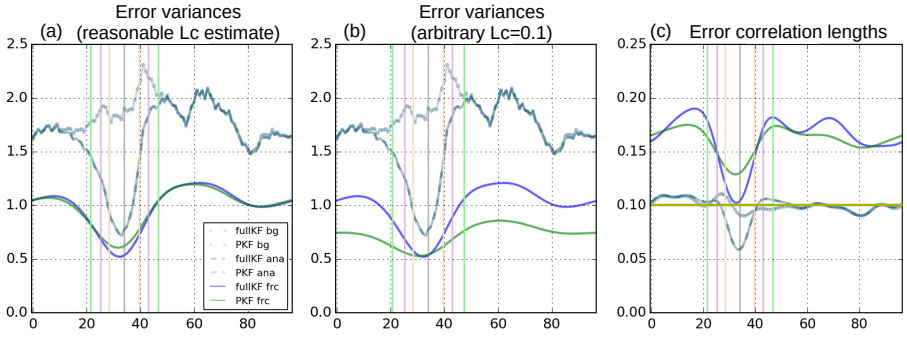

Figure B2. Comparison of idealized 1D experiment for diffusion for different correlation lengths: (a) from reasonable estimate (PKF forecast in (c), same as Fig. B1a), (b) from arbitrarily definition of 0.1=10 gridpoints (mean background in (c)). Plotting convention as in Fig. B1). Figure (c): error correlation length fields of background (dotted), analysis (dashed) and diffusion forecast (solid) for the full KF (blue), reasonable PKF estimate (green) and arbitrary definition (dark yellow), respectively.

B2 Importance of correlation length

The same idealized 1D experiment described in Apx. B1 is used to demonstrate the influence of defined error correlation length on the resulting forecast error variance which has been calculated from the prognostic equation of error standard deviation due to diffusion in Eq. (12). When the PKF forecast error variance after diffusion is calculated with a reasonable estimate of error correlation length in Fig. B2a, it remains accurate compared to the full KF error variance field even for strong diffusion. In this example, this reasonable estimate was achieved by a leading order PKF forecast of error correlation length due to diffusion (e.g. Pannekoucke et al. (2016), their Eq. (24)) shown in Fig. B2c.

In contrast, setting the error correlation length to a significantly lower value, the forecast error variance in Fig. B2b is considerably underestimated after strong diffusion. In this example, an arbitrary constant error correlation length of 0.1 (equivalent to 10 gridpoints) was used throughout the whole diffusion process which represents the mean background error correlation length and thus underestimates the final correlation by about 40% (Fig. B2c). This underestimated correlation results in an overestimation of the reduction of error variance due to diffusion (compare Eq. (12)) and thus in an underestimation of the final forecast error variance of about 25% for most locations (Fig B2b).

Note that the accurate estimate of forecast error variance at the observation location results only because the true forecast error correlation length happens to be 0.1 in this example (Fig. B2c). Thus, the fact that the arbitrary estimate in Fig B2b is more accurate around the observation location than the approximative correlation forecast in Fig.B2a is purely by chance and does not have any conceptual reason.

https://doi.org/10.5194/egusphere-2025-6386
Preprint. Discussion started: 30 December 2025

Appendix C: Real case experiments with different vertical error correlation lengths

Because diffusion is constantly acting on a plume since its emission, the impact of the vertical error correlation length is accumulating over time (compare Sec. 2.2). Consequently, the estimated error correlation length has an increasing impact on forecasted error standard deviation far away from sources which can be seen from a comparison in Fig. C1.

A small vertical error correlation length - here L_{ξ}^{z}=4 vertical model layers (approx. 210 m height at the surface over flat terrain) - induces strong decay of error standard deviations over time which here results in significantly shorter wildfire "uncertainty-plumes" in the forecast of error standard deviation (Fig. C1a-d). For increasing vertical error correlation length - here L_{ξ}^{z}=8 or 10 vertical model layers (approx. 600 m or 865 m height) - the wildfire uncertainty-plumes lengthen and converge to the shape of the wildfire concentration plumes (Fig. C1i-p, compare with Fig. 2) which means that the reduction term in the error diffusion equation Eq. (12) becomes neglectable. Thus, the impact on the error standard deviation forecast is stronger for shorter vertical error standard deviations. The comparison indicates that L_{ξ}^{z}=6 vertical model layers (approx. 385 m height) appears to be a medium vertical error correlation length which balances a reasonable extension of the uncertainty-plumes with a significant reduction compared to concentration-plumes (Fig. C1e-h) and is therefore selected to be discussed more detailed in Sec. 4.

The resulting hourly analysis increments in Fig. C2 are also impacted by the selected vertical error correlation length. In the urban areas, the combination of smaller error standard deviations and more dense observations make the increments generally less influenced by the parametric error fields and therefore less dependent on the vertical error correlation length. In contrast, more significant differences can be found in the sparsely observed regions in the north, where the different lengths of the strong wildfire uncertainty-plumes directly transfer to the spatial patterns of analysis increments. Consequently, the spatial extend of strong analysis increments increases with increasing vertical error correlation length, even if observations induce opposite signs of increments within the same plume (e.g. in the western center of the study area west of Gouin Reservoir at 07 UTC).

https://doi.org/10.5194/egusphere-2025-6386
Preprint. Discussion started: 30 December 2025

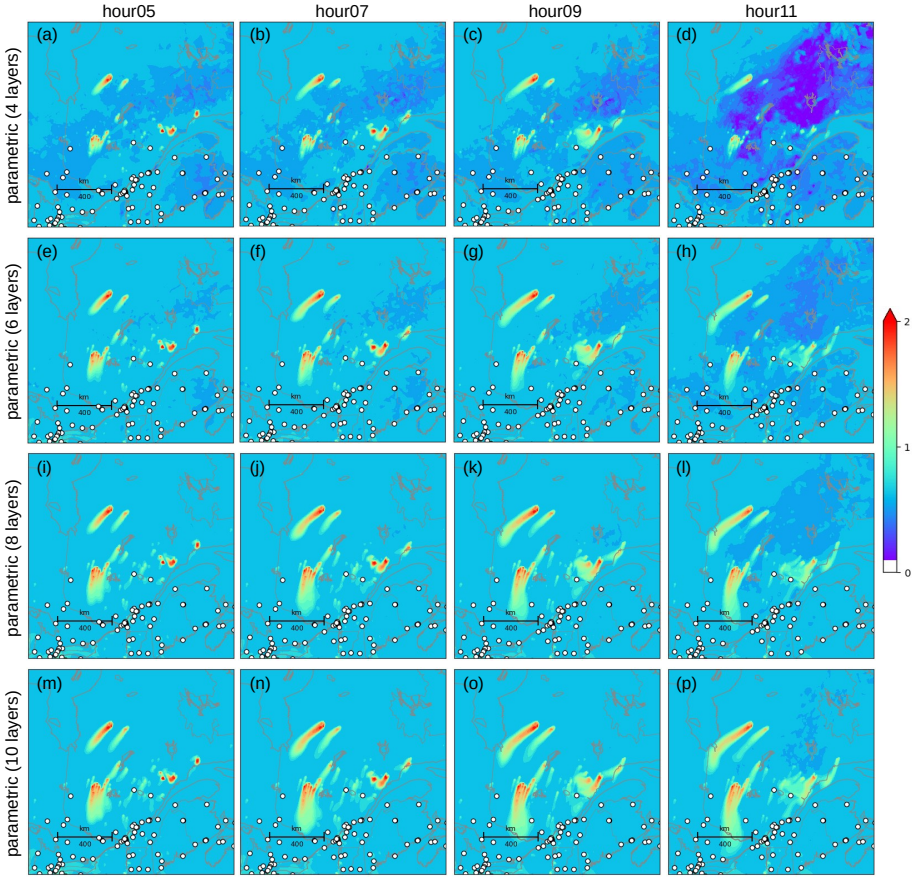

Figure C1. Background error standard deviations fields on June 06, 2023 (logarithmic color code, colorbar labels represent exponent in $\log_{10}(\mu g\, m^{-3})$, hours in UTC) from parametric forecast with different vertical error correlation lengths $L_{\xi}^{z}(\mathbf{x},t)$=4;6;8;10 model layers. Assimilated surface observations are overplotted as white dots.

Author contributions. AV and RM conceptualized the study, AV performed the theoretical derivations, AV and JC did the code implementations in GEM-MACH. JA and RM performed the Objective Analysis. AV wrote the manuscript with contributions from all coauthors.

Competing interests. The authors declare that they have no conflict of interest.

https://doi.org/10.5194/egusphere-2025-6386
Preprint. Discussion started: 30 December 2025

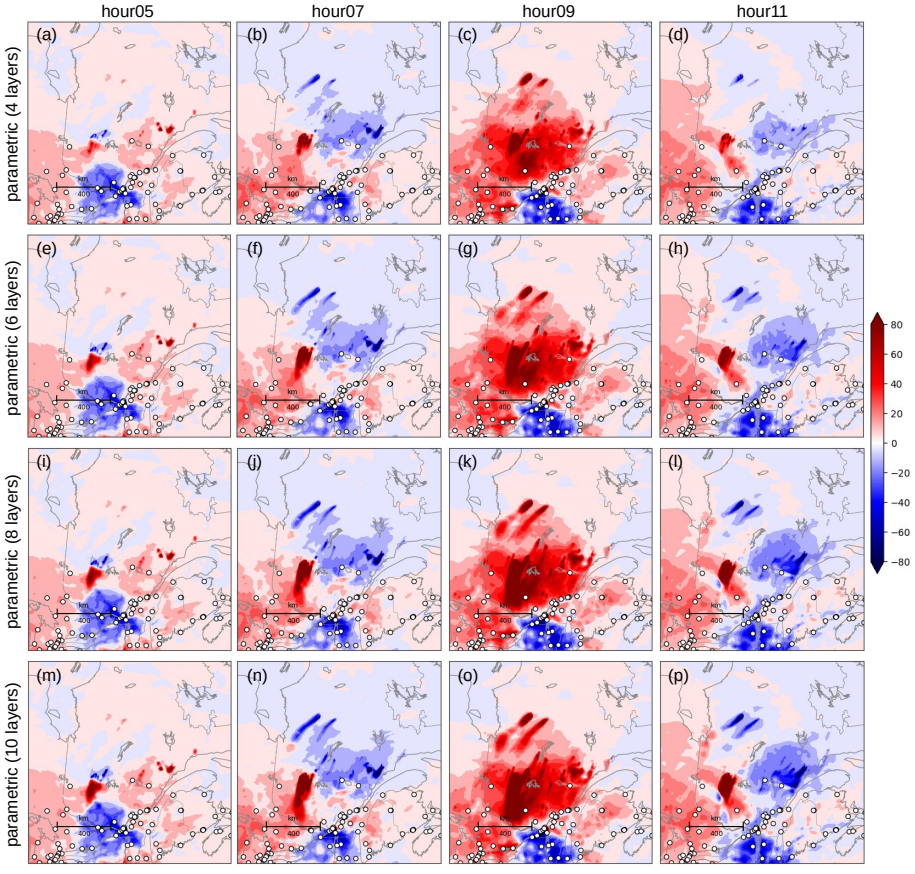

Figure C2. Analysis increments on June 06, 2023 (linear color code, colorbar labels give analysis-background increments in $\mu g\,m^{-3}$, hours in UTC) from parametric forecast with different vertical error correlation lengths $L_\xi^z(\mathbf{x},t)$=4;6;8;10 model layers. Assimilated surface observations are overplotted as white dots.

References

Anderson, K., Chen, J., Englefield, P., Griffin, D., Makar, P. A., and Thompson, D.: The Global Forest Fire Emissions Prediction System version 1.0, Geoscientific Model Development, 17, 7713–7749, https://doi.org/10.5194/gmd-17-7713-2024, 2024.

Brecht, R. and Bihlo, A.: Computing the Ensemble Spread From Deterministic Weather Predictions Using Conditional Generative Adversarial Networks, Geophysical Research Letters, 50, e2022GL101 452, https://doi.org/https://doi.org/10.1029/2022GL101452, e2022GL101452 2022GL101452, 2023.

Buehner, M., McTaggart-Cowan, R., Beaulne, A., Charette, C., Garand, L., Heilliette, S., Lapalme, E., Laroche, S., Macpherson, S. R., Morneau, J., and Zadra, A.: Implementation of Deterministic Weather Forecasting Systems Based on Ensemble–Variational Data Assimilation at Environment Canada. Part I: The Global System, Monthly Weather Review, 143, 2532 – 2559, https://doi.org/10.1175/MWR-D-14-00354.1, 2015.

https://doi.org/10.5194/egusphere-2025-6386
Preprint. Discussion started: 30 December 2025

Byrne, B., Liu, J., Bowman, K., Pascolini-Campbell, M., Chatterjee, A., Pandey, S., Miyazaki, K., van der Werf, G., Wunch, D., Wennberg, P., Roehl, C., and Sinha, S.: Carbon emissions from the 2023 Canadian wildfires, Nature, 633, 835–839, https://doi.org/10.1038/s41586-024-07878-z, 2024.

Chen, H., Kaufman, J. S., Chen, C., Wang, J., Maier, A., van Dijk, A., Slipp, N., Rana, J., MacIntyre, E., Su, Y., Kim, J., and Benmarhnia, T.: Impact of the 2023 wildfire smoke episodes in Ontario, Canada, on asthma and other health outcomes: an interrupted time-series analysis, CMAJ, 197, E465–E477, https://doi.org/10.1503/cmaj.241506, 2025.

Chen, J., Anderson, K., Pavlovic, R., Moran, M. D., Englefield, P., Thompson, D. K., Munoz-Alpizar, R., and Landry, H.: The FireWork v2.0 air quality forecast system with biomass burning emissions from the Canadian Forest Fire Emissions Prediction System v2.03, Geoscientific Model Development, 12, 3283–3310, https://doi.org/10.5194/gmd-12-3283-2019, 2019.

Cohn, S. E.: Dynamics of Short-Term Univariate Forecast Error Covariances, Monthly Weather Review, 121, 3123 – 3149, https://doi.org/10.1175/1520-0493(1993)121<3123:DOSTUF>2.0.CO;2, 1993.

Colette, A., Collin, G., Besson, F., Blot, E., Guidard, V., Meleux, F., Royer, A., Petiot, V., Miller, C., Fermond, O., Jeant, A., Adani, M., Arteta, J., Benedictow, A., Bergström, R., Bowdalo, D., Brandt, J., Briganti, G., Carvalho, A. C., Christensen, J. H., Couvidat, F., D'Elia, I., D'Isidoro, M., Denier van der Gon, H., Descombes, G., Di Tomaso, E., Douros, J., Escribano, J., Eskes, H., Fagerli, H., Fatahi, Y., Flemming, J., Friese, E., Frohn, L., Gauss, M., Geels, C., Guarnieri, G., Guevara, M., Guion, A., Guth, J., Hänninen, R., Hansen, K., Im, U., Janssen, R., Jeoffrion, M., Joly, M., Jones, L., Jorba, O., Kadantsev, E., Kahnert, M., Kaminski, J. W., Kouznetsov, R., Kranenburg, R., Kuenen, J., Lange, A. C., Langner, J., Lannuque, V., Macchia, F., Manders, A., Mircea, M., Nyiri, A., Olid, M., Pérez García-Pando, C., Palamarchuk, Y., Piersanti, A., Raux, B., Razinger, M., Robertson, L., Segers, A., Schaap, M., Siljamo, P., Simpson, D., Sofiev, M., Stangel, A., Struzewska, J., Tena, C., Timmermans, R., Tsikerdekis, T., Tsyro, S., Tyuryakov, S., Ung, A., Uppstu, A., Valdebenito, A., van Velthoven, P., Vitali, L., Ye, Z., Peuch, V.-H., and Rouïl, L.: Copernicus Atmosphere Monitoring Service – Regional Air Quality Production System v1.0, Geoscientific Model Development, 18, 6835–6883, https://doi.org/10.5194/gmd-18-6835-2025, 2025.

Epstein, E. S.: Stochastic dynamic prediction, Tellus, 21, 739–759, https://doi.org/https://doi.org/10.1111/j.2153-3490.1969.tb00483.x, 1969.

Eskes, H. J., Velthoven, P. F. J. V., Valks, P. J. M., and Kelder, H. M.: Assimilation of GOME total-ozone satellite observations in a three-dimensional tracer-transport model, Quarterly Journal of the Royal Meteorological Society, 129, 1663–1681, https://doi.org/https://doi.org/10.1256/qj.02.14, 2003.

Flood, V. A., Strong, K., Whaley, C. H., Chen, J., Wunch, D., Drummond, J. R., Colebatch, O., Gillespie, L., and Mostafavi Pak, N.: The Impact of the 2023 Canadian Forest Fires on Air Quality in Southern Ontario, Journal of Geophysical Research: Atmospheres, 130, e2024JD042 254, https://doi.org/https://doi.org/10.1029/2024JD042254, e2024JD042254 2024JD042254, 2025.

Gaspari, G. and Cohn, S. E.: Construction of correlation functions in two and three dimensions, Quarterly Journal of the Royal Meteorological Society, 125, 723–757, https://doi.org/https://doi.org/10.1002/qj.49712555417, 1999.

Gilpin, S., Matsuo, T., and Cohn, S. E.: Inaccuracy of the variance evolution associated with discrete covariance propagation, Quarterly Journal of the Royal Meteorological Society, n/a, e5016, https://doi.org/https://doi.org/10.1002/qj.5016, 2025.

Griffin, D., Sioris, C., Chen, J., Dickson, N., Kovachik, A., de Graaf, M., Nanda, S., Veefkind, P., Dammers, E., McLinden, C. A., Makar, P., and Akingunola, A.: The 2018 fire season in North America as seen by TROPOMI: aerosol layer height intercomparisons and evaluation of model-derived plume heights, Atmospheric Measurement Techniques, 13, 1427–1445, https://doi.org/10.5194/amt-13-1427-2020, 2020.

Henderson, S. B.: Wildfire smoke air pollution: new approaches needed to protect people affected, CMAJ, 197, E483–E484, https://doi.org/10.1503/cmaj.250510, 2025.

https://doi.org/10.5194/egusphere-2025-6386
Preprint. Discussion started: 30 December 2025

Jain, P., Barber, Q. E., Taylor, S., Whitman, E., Acuna, D. C., Boulanger, Y., and et al.: Drivers and impacts of the record-breaking 2023 wildfire season in Canada, Nature Communications, 15, 6764, https://doi.org/10.1038/s41467-024-51154-7, 2024.

Kaiser, J. W., Heil, A., Andreae, M. O., Benedetti, A., Chubarova, N., Jones, L., Morcrette, J.-J., Razinger, M., Schultz, M. G., Suttie, M., and van der Werf, G. R.: Biomass burning emissions estimated with a global fire assimilation system based on observed fire radiative power, Biogeosciences, 9, 527–554, https://doi.org/10.5194/bg-9-527-2012, 2012.

Ke, Z., Wang, Y., Zou, Y., Song, Y., and Liu, Y.: Global Wildfire Plume-Rise Data Set and Parameterizations for Climate Model Applications, Journal of Geophysical Research: Atmospheres, 126, e2020JD033 085, https://doi.org/https://doi.org/10.1029/2020JD033085, e2020JD033085 2020JD033085, 2021.

Khattatov, B. V., Lamarque, J.-F., Lyjak, L. V., Menard, R., Levelt, P., Tie, X., Brasseur, G. P., and Gille, J. C.: Assimilation of satellite observations of long-lived chemical species in global chemistry transport models, Journal of Geophysical Research: Atmospheres, 105, 29 135–29 144, https://doi.org/https://doi.org/10.1029/2000JD900466, 2000.

Kong, L., Tang, X., Zhu, J., Wang, Z., Li, J., Wu, H., Wu, Q., Chen, H., Zhu, L., Wang, W., Liu, B., Wang, Q., Chen, D., Pan, Y., Song, T., Li, F., Zheng, H., Jia, G., Lu, M., Wu, L., and Carmichael, G. R.: A 6-year-long (2013–2018) high-resolution air quality reanalysis dataset in China based on the assimilation of surface observations from CNEMC, Earth System Science Data, 13, 529–570, https://doi.org/10.5194/essd-13-529-2021, 2021.

Leutbecher, M.: Ensemble size: How suboptimal is less than infinity?, Quarterly Journal of the Royal Meteorological Society, 145, 107–128, 2019.

Li, L., Carver, R., Lopez-Gomez, I., Sha, F., and Anderson, J.: Generative emulation of weather forecast ensembles with diffusion models, Science Advances, 10, eadk4489, https://doi.org/10.1126/sciadv.adk4489, 2024.

Ménard, R., Cossette, J.-F., and Deshaies-Jacques, M.: On the Complementary Role of Data Assimilation and Machine Learning: An Example Derived from Air Quality Analysis, in: Computational Science – ICCS 2020, edited by Krzhizhanovskaya, V. V., Závodszky, G., Lees, M. H., Dongarra, J. J., Sloot, P. M. A., Brissos, S., and Teixeira, J., pp. 212–224, Springer International Publishing, Cham, ISBN 978-3-030-50433-5, 2020.

Ménard, R. and Chang, L.-P.: Assimilation of Stratospheric Chemical Tracer Observations Using a Kalman Filter. Part II: ^{2}-Validated Results and Analysis of Variance and Correlation Dynamics, Monthly Weather Review, 128, 2672 – 2686, https://doi.org/10.1175/1520-0493(2000)128<2672:AOSCTO>2.0.CO;2, 2000.

Ménard, R. and Deshaies-Jacques, M.: Evaluation of Analysis by Cross-Validation. Part I: Using Verification Metrics, Atmosphere, 9, https://doi.org/10.3390/atmos9030086, 2018a.

Ménard, R. and Deshaies-Jacques, M.: Evaluation of Analysis by Cross-Validation, Part II: Diagnostic and Optimization of Analysis Error Covariance, Atmosphere, 9, https://doi.org/10.3390/atmos9020070, 2018b.

Ménard, R., Skachko, S., and Pannekoucke, O.: Numerical discretization causing error variance loss and the need for inflation, Quarterly Journal of the Royal Meteorological Society, 147, 3498–3520, https://doi.org/https://doi.org/10.1002/qj.4139, 2021.

Pannekoucke, O., Ricci, S., Barthelemy, S., Ménard, R., and Thual, O.: Parametric Kalman filter for chemical transport models, Tellus A: Dynamic Meteorology and Oceanography, 68, 31 547, https://doi.org/10.3402/tellusa.v68.31547, 2016.

Pannekoucke, O., Bocquet, M., and Ménard, R.: Parametric covariance dynamics for the nonlinear diffusive Burgers equation, Nonlinear Processes in Geophysics, 25, 481–495, https://doi.org/10.5194/npg-25-481-2018, 2018.

https://doi.org/10.5194/egusphere-2025-6386
Preprint. Discussion started: 30 December 2025

Pannekoucke, O., Ménard, R., El Aabaribaoune, M., and Plu, M.: A methodology to obtain model-error covariances due to the discretization scheme from the parametric Kalman filter perspective, Nonlinear Processes in Geophysics, 28, 1–22, https://doi.org/10.5194/npg-28-1-2021, 2021.

Park, S.-Y., Dash, U. K., Yu, J., Yumimoto, K., Uno, I., and Song, C. H.: Implementation of an ensemble Kalman filter in the Community Multiscale Air Quality model (CMAQ model v5.1) for data assimilation of ground-level $PM_{2.5}$, Geoscientific Model Development, 15, 2773–2790, https://doi.org/10.5194/gmd-15-2773-2022, 2022.

Pendergrass, D. C., Jacob, D. J., Nesser, H., Varon, D. J., Sulprizio, M., Miyazaki, K., and Bowman, K. W.: CHEEREIO 1.0: a versatile and user-friendly ensemble-based chemical data assimilation and emissions inversion platform for the GEOS-Chem chemical transport model, Geoscientific Model Development, 16, 4793–4810, https://doi.org/10.5194/gmd-16-4793-2023, 2023.

Perrot, A., Pannekoucke, O., and Guidard, V.: Toward a multivariate formulation of the parametric Kalman filter assimilation: application to a simplified chemical transport model, Nonlinear Processes in Geophysics, 30, 139–166, https://doi.org/10.5194/npg-30-139-2023, 2023.

Rochoux, M., Delmotte, B., Cuenot, B., Ricci, S., and Trouvé, A.: Regional-scale simulations of wildland fire spread informed by real-time flame front observations, Proceedings of the Combustion Institute, 34, 2641–2647, https://doi.org/https://doi.org/10.1016/j.proci.2012.06.090, 2013.

Rochoux, M. C., Emery, C., Ricci, S., Cuenot, B., and Trouvé, A.: Towards predictive data-driven simulations of wildfire spread – Part II: Ensemble Kalman Filter for the state estimation of a front-tracking simulator of wildfire spread, Natural Hazards and Earth System Sciences, 15, 1721–1739, https://doi.org/10.5194/nhess-15-1721-2015, 2015.

Sabathier, M., Pannekoucke, O., Maget, V., and Dahmen, N.: Boundary Conditions for the Parametric Kalman Filter Forecast, Journal of Advances in Modeling Earth Systems, 15, e2022MS003 462, https://doi.org/https://doi.org/10.1029/2022MS003462, e2022MS003462 2022MS003462, 2023.

Sacco, M. A., Ruiz, J. J., Pulido, M., and Tandeo, P.: Evaluation of machine learning techniques for forecast uncertainty quantification, Quarterly Journal of the Royal Meteorological Society, 148, 3470–3490, https://doi.org/https://doi.org/10.1002/qj.4362, 2022.

Sitwell, M.: EnsAI: An Emulator for Atmospheric Chemical Ensembles, https://arxiv.org/abs/2504.16024, 2025.

Srivas, T., de Callafon, R. A., Crawl, D., and Altintas, I.: Data Assimilation of Wildfires with Fuel Adjustment Factors in farsite using Ensemble Kalman Filtering, Procedia Computer Science, 108, 1572–1581, https://doi.org/https://doi.org/10.1016/j.procs.2017.05.197, international Conference on Computational Science, ICCS 2017, 12-14 June 2017, Zurich, Switzerland, 2017.

Sun, W., Liu, Z., Chen, D., Zhao, P., and Chen, M.: Development and application of the WRFDA-Chem three-dimensional variational (3DVAR) system: aiming to improve air quality forecasting and diagnose model deficiencies, Atmospheric Chemistry and Physics, 20, 9311–9329, https://doi.org/10.5194/acp-20-9311-2020, 2020.

Vogel, A. and Elbern, H.: Identifying forecast uncertainties for biogenic gases in the Po Valley related to model configuration in EURAD-IM during PEGASOS 2012, Atmospheric Chemistry and Physics, 21, 4039–4057, https://doi.org/10.5194/acp-21-4039-2021, 2021a.

Vogel, A. and Elbern, H.: Efficient ensemble generation for uncertain correlated parameters in atmospheric chemical models: a case study for biogenic emissions from EURAD-IM version 5, Geoscientific Model Development, 14, 5583–5605, https://doi.org/10.5194/gmd-14-5583-2021, 2021b.

Vogel, A., Ménard, R., Abu, J., and Chen, J.: Dispersion dynamics of wildfire aerosol for prognostic error variance evolution and improved assimilation, in: Air Pollution Modeling and its Application XXX, edited by Mensink, C. and Im, U., Springer Cham, ISBN 978-3-032-02971-3, 2026.

https://doi.org/10.5194/egusphere-2025-6386
Preprint. Discussion started: 30 December 2025

Voshtani, S., Ménard, R., Walker, T. W., and Hakami, A.: Assimilation of GOSAT Methane in the Hemispheric CMAQ; Part I: Design of the Assimilation System, Remote Sensing, 14, https://doi.org/10.3390/rs14020371, 2022.

Wang, H., Martin, C., Barré, J., Li, R., Weygandt, S., Huang, J., Tang, Y., Choi, H., Tangborn, A., Wang, K., Liu, H., and Lee, J.: $PM_{PM2.5}$ Assimilation within JEDI for NOAA's Regional Air Quality Model (AQMv7): Application to the September 2020 Western U.S. Wildfires, EGUsphere, 2025, 1–31, https://doi.org/10.5194/egusphere-2025-4098, 2025.

Wang, Z., Wang, Z., Zou, Z., Chen, X., Wu, H., Wang, W., Su, H., Li, F., Xu, W., Liu, Z., and Zhu, J.: Severe Global Environmental Issues Caused by Canada's Record-Breaking Wildfires in 2023, Advances in Atmospheric Sciences, 41, 565–571, 2024.

Wu, T., Zhang, Q., Zhu, J., Wu, J., Dai, J., and Zhang, Y.: Dynamic Correction of Forest Fire Spread Prediction using Observation Error Covariance Matrix Estimation Technique based on FLC-GRU, Fire Ecology, 20, https://doi.org/10.21203/rs.3.rs-3972535/v1, 2024.

Zhang, Q., Wang, Y., Xiao, Q., and et al.: Long-range PM2.5 pollution and health impacts from the 2023 Canadian wildfires, Nature, 645, 672–678, https://doi.org/10.1038/s41586-025-09482-1, 2025.

Zhou, T., Ding, L., Ji, J., and Luo, S.: VWETKF for wildfire propagation prediction employing observations with missing values and/or spatial variations of error variance, Proceedings of the Combustion Institute, 38, 5091–5099, https://doi.org/https://doi.org/10.1016/j.proci.2020.05.028, 2021.